Supplementary Information for

Phononic Modulation of Spin-Lattice Relaxation in Molecular Qubit Frameworks

Aimei Zhou,[1,2,3] Denan Li,[4] Mingshu Tan,[5] Yanpei Lv,[6,7] Simin Pang[6,7], Xinxing Zhao,[8] Zhifu Shi,[8] Jun Zhang,[6,7] Feng Jin,[5] Shi Liu,[2,3,4] Lei Sun[2,3,4,*]

[1]Department of Chemistry, Zhejiang University, Hangzhou 310058, Zhejiang Province, China

[2]Department of Chemistry, School of Science and Research Center for Industries of the Future, Westlake University, Hangzhou 310030, Zhejiang Province, China

[3]Institute of Natural Sciences, Westlake Institute for Advanced Study, Hangzhou 310024, Zhejiang Province, China

[4]Department of Physics, School of Science and Research Center for Industries of the Future, Westlake University, Hangzhou 310030, Zhejiang Province, China

[5]Beijing National Laboratory for Condensed Matter Physics, Institute of Physics, Chinese Academy of Sciences, Beijing 100190, China

[6]State Key Laboratory of Superlattices and Microstructures, Institute of Semiconductors, Chinese Academy of Sciences, Beijing 100083, China

[7]Center of Materials Science and Optoelectronics Engineering, University of Chinese Academy of Sciences, Beijing 100049, China

[8]CIQTEK Co., Ltd, Hefei 230031, Anhui Province, China

*Correspondence to Lei Sun

Email: sunlei@westlake.edu.cn

Table of contents

1. Materials

All commercially available chemicals were used without further purification unless otherwise noted. 1,2-Dimethoxybenzene and anhydrous $FeCl_3$ were purchased from Macklin. $Mg(acetate)_2 \cdot 4H_2O$ (99%) was purchased from Aladdin. Titanium (IV) isopropoxide (≥97%) was purchased from Sigma-Aldrich. Triethylamine was purchased from Sinopharm and purified by a solvent purification system. Acetic acid (≥99.5%), methanol (≥99.5%), ethanol (≥99.7%), acetone (≥99.5%), *N, N*-Dimethylformamide and dichloromethane (≥99.5%) were purchased from Sinopharm. Hydrobromic acid (47%) was purchased from TCI. 2,3,6,7,10,11-hexatriphenylene (HHTP),[1,2] MgHOTP,[3] and TiHOTP[4] were synthesized based on literature procedures.

2. Powder X-ray diffraction

Powder X-ray diffraction (PXRD) was performed on Bruker Advance D8 diffractometer with a scan rate of 0.2 seconds per step and a step size of 0.02°. Samples were tested on a zero-background silicon crystal plate.
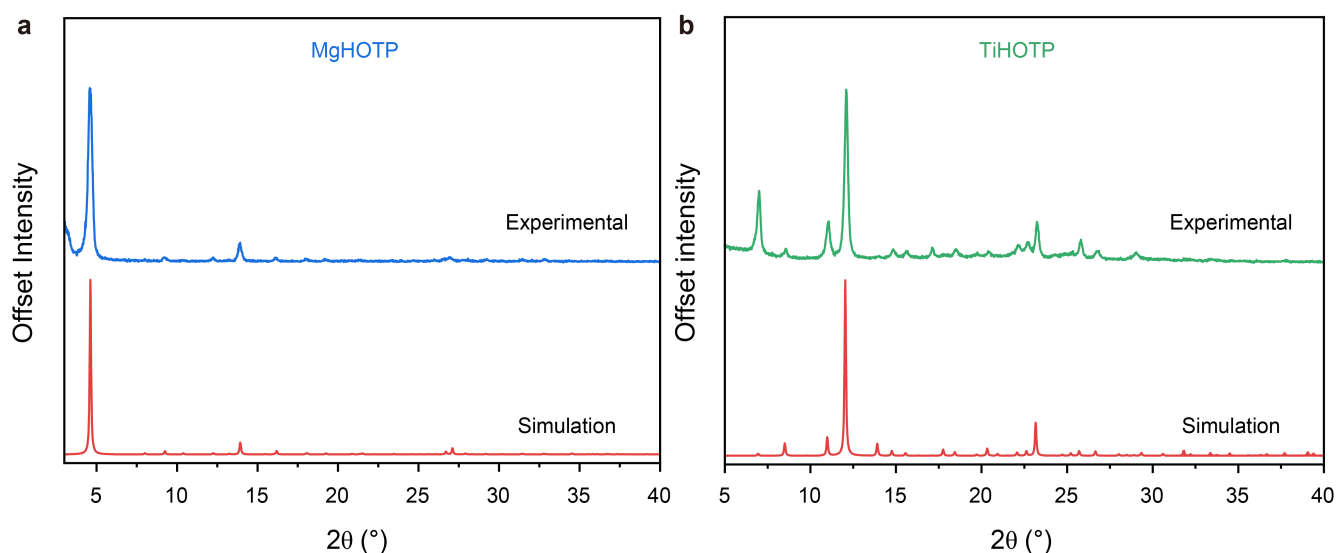
Supplementary Figure 1. Experimental and simulated PXRD patterns of a, MgHOTP and b, TiHOTP. Red lines represent simulated patterns based on single crystal structures of MgHOTP and TiHOTP.

3. Continuous-wave (CW) EPR spectra
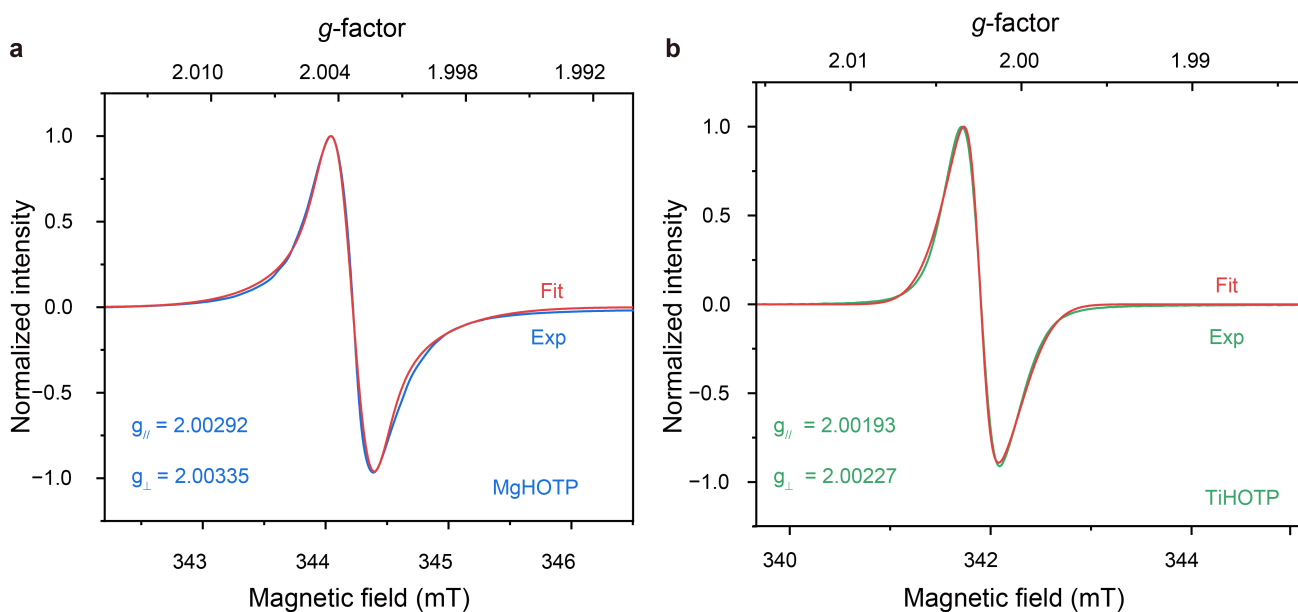
Supplementary Figure 2. X-band CW EPR spectra of a, MgHOTP and b, TiHOTP. Red lines represent fitting results. The spectra were fitted by EasySpin 6.0.0[5] in MATLAB R2023b.
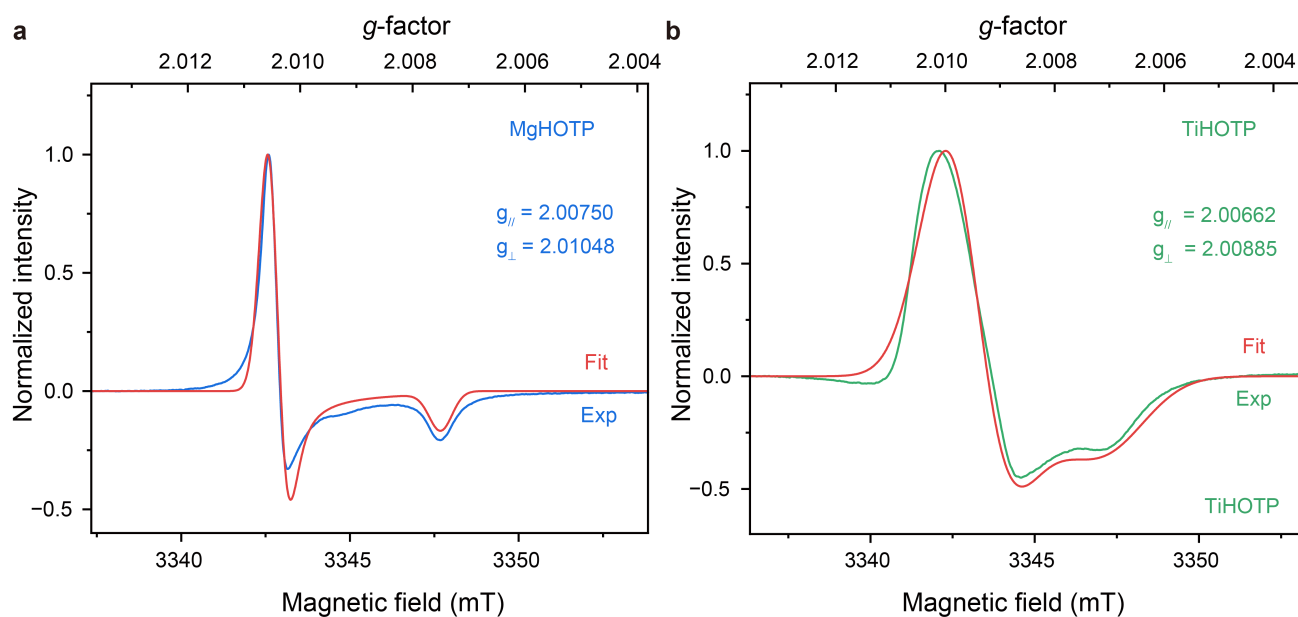
Supplementary Figure 3. W-band CW spectra of a, MgHOTP and b, TiHOTP. Red lines represent fitting results. The spectra were fitted by EasySpin 6.0.0[5] in MATLAB R2023b. We encountered a difficulty in accurately calibrating the magnetic field due to technical issues, so the g-factors obtained from W-band CW EPR spectra are slightly higher than those obtained from X-band CW EPR spectra.

Supplementary Table 1. Comparison between isotropic g-factors (g_{iso}) of MQFs and the free electron value (g_e).

MQFs	$g_{//}$	$g_{\perp}$	$g_{iso} = \sqrt{\frac{1}{3}(g_{\parallel}^2 + 2g_{\perp}^2)}$	$\lvert g_{iso} - g_e \rvert$
TiHOTP	2.00193	2.00227	2.00216	0.00016
MgHOTP	2.00292	2.00335	2.00321	0.00089
MgHOTP-D$_2$O	2.00245	2.00371	2.00329	0.00097

4. Spin density distributions of HOTP radicals

As shown in Supplementary Figure 4, HOTP may undergo up to six-electron oxidation to transform into quinone (HOTP-6) through five intermediates (HOTP-1 to HOTP-5). The 1-, 3-, and 5-electron oxidation products possess unpaired electrons that resemble semiquinone-like radicals. DFT calculations reveal that the spin density concentrates at oxygen atoms and slightly distributes to carbon atoms due to conjugation (Fig. 1c, 1d, Supplementary Figure 5, and Table 2).
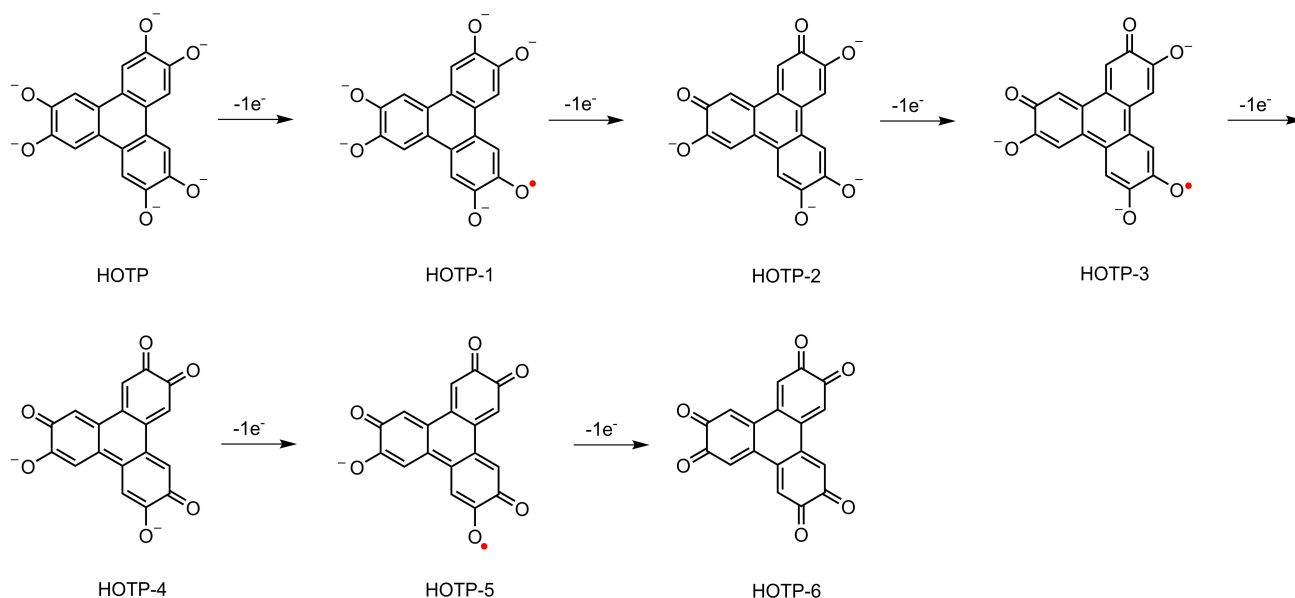
Supplementary Figure 4. HOTP and oxidation products.
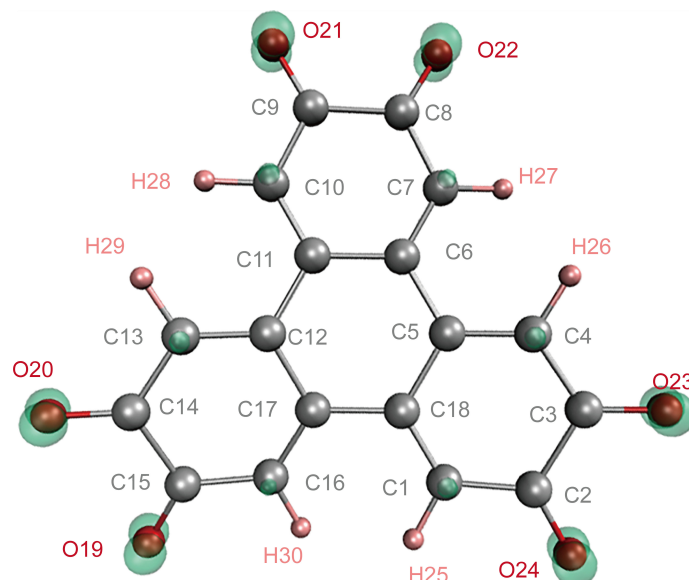
Supplementary Figure 5. Spin density distribution maps of HOTP-5. Grey, pink, and red spheres represent C, H, and O, respectively. Green and blue clouds represent spin up and spin down electrons, respectively. The labels near atoms correspond to those in Supplementary Table 1. (isosurfaces = 0.01)

7

Supplementary Table 2. Population of spin density on each atom in various forms of HOTP radicals. Positive values represent spin up density, and negative values represent spin down density. The labels of atoms are shown in Supplementary Figure 5.

Atomic label	HOTP-1/%	HOTP-3/%	HOTP-5/%
1(C)	-0.2879	-0.44144	5.888513
2(C)	-2.03389	-2.66491	1.670923
3(C)	-1.99802	-2.65758	1.659209
4(C)	-0.18943	-0.41309	5.680788
5(C)	-1.91786	-2.6454	0.983241
6(C)	2.126517	4.902069	0.979956
7(C)	1.61833	1.130617	5.680819
8(C)	3.535344	4.346734	1.663385
9(C)	2.410489	3.794141	1.672888
10(C)	1.681175	3.053209	5.850866
11(C)	2.283015	3.48732	1.008374
12(C)	2.327696	3.505029	1.040106
13(C)	1.687913	3.055698	5.51862
14(C)	2.083721	3.806882	1.571943
15(C)	0.09243	4.351733	1.574764
16(C)	1.153331	1.134478	5.555352
17(C)	2.112033	4.899224	1.079707
18(C)	-1.92927	-2.64176	1.0492
19(O)	-17.4374	9.24073	7.758512
20(O)	3.697925	8.074336	7.724894
21(O)	4.715094	8.042827	8.101833
22(O)	30.64331	9.231689	8.019174
23(O)	-3.82331	-6.03715	8.03335
24(O)	-3.90791	-6.05448	8.141456
25(H)	-0.06483	0.026561	0.377115
26(H)	0.121741	0.02864	0.335391
27(H)	2.02684	0.003723	0.339711
28(H)	0.092435	0.162522	0.368973
29(H)	0.084674	0.162379	0.329877
30(H)	-1.91622	0.003664	0.34106

5. X-band pulse EPR spectroscopy

Nutation experiments

Nutation experiments were performed with a three-pulse sequence (nutation pulse – T – π/2 – τ – π – τ – echo) with 512 data points in various microwave attenuations (0, 3, 6, 9, 12, 15, and 18 dB). The duration of the nutation pulse began at 6 ns and increased by 2 ns with each subsequent step. T and τ were set to 400 and 200 ns, respectively. The background noise was canceled by four-step phase cycling with pulse phases of (+x, -x, +x) (+x, +x, +x) (-x, -x, +x) and (-x, +x, +x). Fast Fourier transform (FFT) in Origin 2023b was used to transform nutation curves from the time domain to the frequency domain after baseline correction with cubic polynomials, apodization with the Hamming window function, and zero-filling. Rabi frequencies recorded at the frequency of the peak after FFT are different at different microwave attenuations, which are plotted against the ratio between the magnetic field of the output microwave (B_{out}, after attenuation) and the input microwave (B_{in}, before attenuation), which is $10^{\frac{-Attenuation}{20\,dB}}$ with *Attenuation* the microwave attenuation in the unit of dB.
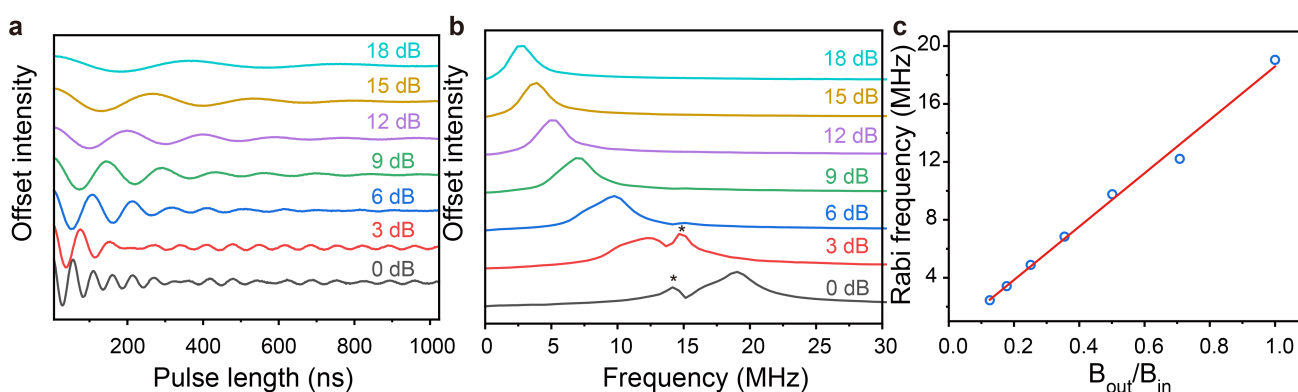
Supplementary Figure 6. Results of nutation experiments of TiHOTP. a, Time-domain nutation curves at various microwave attenuations. b, Frequency-domain nutation curves. The peaks marked by asterisk signs are the results of the Hartman–Hahn effect of the processing ^{1}H nucleus.[6] c, Plots of Rabi frequency vs. normalized microwave magnetic field strength showing linear relationships.

Inversion recovery

When fitting inversion recovery curves collected at low temperatures, the first data point, i.e. the one associated with the shortest T, was not involved to avoid the experimental artefact. Specifically, the long T_1 at low temperature necessitates the use of a large step-increment of T during the inversion recovery experiment. As such, the bi-exponential decay fitting would give rise to bad fits in the long-T regime. As T_1 is extracted from the slow exponential decay process, this would introduce large errors to T_1. Thus, it is legitimate to eliminate the first data point for fitting.

CP-ESEEM spectroscopy

The combination-peak (CP) electron spin echo envelope modulation (ESEEM) spectroscopy was conducted with a

four-pulse sequence (π/2 – τ –π/2 – T – π – T –π/2 – τ – echo) with 512 data points at 344.8 mT. T started at 500 ns and was incremented 8 ns per step. Eight-step phase cycling was employed with pulse phases of (+x, +x, +x, +x) (-x, +x, +x, +x) (+x, -x, +x, +x) (-x, -x, +x, +x) (+x, +x, +x, -x) (-x, +x, +x, -x) (+x, -x, +x, -x) (-x, -x, +x, -x) to cancel background, unwanted echoes, and the defense pulse. τ was fixed at 170 ns. Integration of the echo was plotted against the delay time, T, giving an oscillatory time-domain CP-ESEEM spectrum. The time-domain CP-ESEEM spectrum was background-corrected with polynomial fitting, apodized with the Hamming window function, zero-filled, and transformed to frequency domain by FFT.
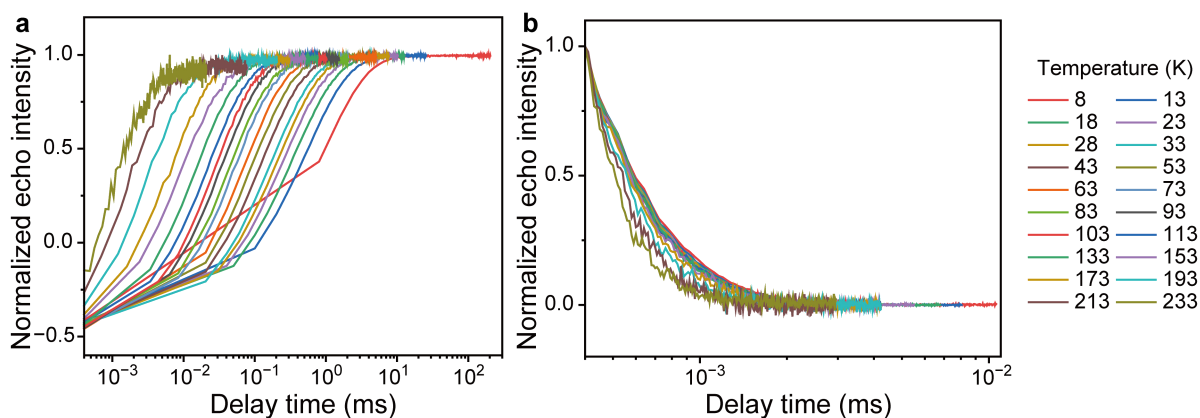
Supplementary Figure 7. a, Inversion recovery curves and b, Hahn echo decay curves of MgHOTP at various temperatures.
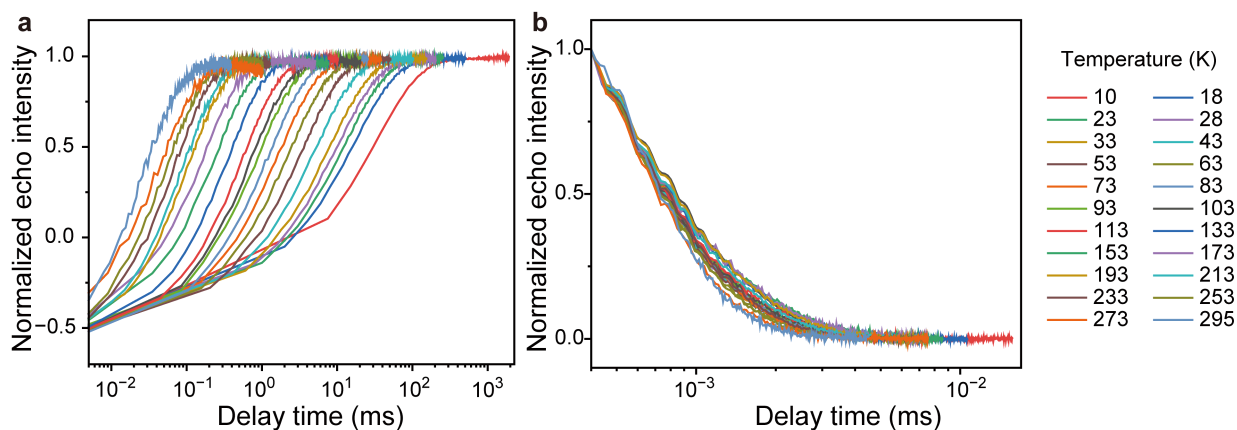
Supplementary Figure 8. a, Inversion recovery curves and b, Hahn echo decay curves of TiHOTP at various temperatures.

Supplementary Table 3. T_1 and T_m of MgHOTP at various temperatures.

Temperature (K)	T_1 (µs)	T_s (µs)	T_m (ns)
8	3.96 (2) × 10³	1.17 (4) × 10³	3.52 (3) × 10²
13	1.32 (2) × 10³	3.84 (8) × 10³	3.35 (3) × 10²
18	8.4 (1) × 10²	2.27 (5) × 10²	3.21 (2) × 10²
23	6.5 (1) × 10²	1.77 (4) × 10²	3.14 (2) × 10²
28	4.83 (7) × 10²	1.37 (3) × 10²	3.08 (2) × 10²
33	3.99 (5) × 10²	1.10 (2) × 10²	3.02 (2) × 10²
43	2.76 (4) × 10²	6.63 (2) × 10¹	2.97 (2) × 10²
53	1.92 (3) × 10²	4.6 (1) × 10¹	2.93 (2) × 10²
63	1.44 (2) × 10²	3.5 (1) × 10¹	2.92 (2) × 10²
73	1.21 (3) × 10²	3.3 (1) × 10¹	2.93 (2) × 10²
83	9.7 (3) × 10¹	2.7 (1) × 10¹	2.93 (2) × 10²
93	6.7 (1) × 10¹	1.76 (7) × 10¹	2.94 (2) × 10²
103	5.6 (1) × 10¹	1.61 (7) × 10¹	2.94 (2) × 10²
113	5.3 (1) × 10¹	1.46 (3) × 10¹	2.96 (2) × 10²
133	3.34 (8) × 10¹	8.6 (4)	2.94 (2) × 10²
153	2.67 (9) × 10¹	6.3 (2)	2.91 (2) × 10²
173	1.26 (4) × 10¹	3.3 (2)	2.79 (2) × 10²
193	8.1 (5)	2.2 (2)	2.62 (2) × 10²
213	4.6 (7)	1.5 (2)	2.32 (3) × 10²
233	1.7 (2)	5.5 (2)	194(3) × 10²

Supplementary Table 4. T_1 and T_m of TiHOTP at various temperatures.

Temperature (K)	T_1 (μs)	T_s (μs)	T_m (ns)
10	8.3 (2) × 10⁴	2.55 (8) × 10⁴	6.21 (2) × 10²
18	3.46 (8) × 10⁴	1.06 (4) × 10⁴	5.82 (2) × 10²
23	2.32 (3) × 10⁴	6.4 (2) × 10³	5.76 (2) × 10²
28	1.74 (3) × 10⁴	4.7 (2) × 10³	5.65 (4) × 10²
33	1.28 (1) × 10⁴	3.2 (1) × 10³	5.64 (4) × 10²
43	8.2 (1) × 10³	2.2 (1) × 10³	5.67 (4) × 10²
53	4.98 (5) × 10³	1.12 (5) × 10³	5.59 (3) × 10²
63	3.57 (4) × 10³	9.2 (4) × 10²	5.38 (3) × 10²
73	2.56 (5) × 10³	7.3 (5) × 10²	5.79 (3) × 10²
83	1.69 (2) × 10³	2.6 (1) × 10²	5.98 (4) × 10²
93	1.27 (2) × 10³	2.6 (2) × 10²	6.09 (5) × 10²
103	9.6 (1) × 10²	1.8 (2) × 10²	6.13 (5) × 10²
113	7.44 (9) × 10²	1.7 (2) × 10²	6.36 (6) × 10²
133	4.36 (5) × 10²	7.5 (8) × 10¹	6.97 (7) × 10²
153	2.91 (4) × 10²	4.7 (7) × 10¹	7.29 (8) × 10²
173	2.02 (4) × 10²	2.5 (6) × 10¹	7.33 (8) × 10²
193	1.84 (8) × 10²	7.2 (4) × 10¹	7.03 (5) × 10²
213	1.23 (3) × 10²	4.3 (4) × 101²	6.59 (4) × 10²
233	8.6 (2) × 10¹	1.9 (4) × 10¹	5.87 (3) × 10²
253	7.0 (2) × 10¹	1.5 (3) × 10¹	5.26 (2) × 10²
273	5.4 (1) × 10¹	7.4 (4)	4.80 (2) × 10²
294	4.1 (3) × 10¹	1.6 (3) × 10¹	4.55 (3) × 10²

6. Analysis of spin decoherence mechanisms (Supplementary Note 6)

As discussed in the main text, we divided the temperature dependencies of T_m for MgHOTP and TiHOTP collected at X-band into three sections. In the high-temperature region (above 113 K for MgHOTP and above 173 K for TiHOTP), although the T_m is much shorter than the T_1, it seems to be closely related to the T_1. Based on a decoherence model proposed by Wilson et al.[7], we used the following equation to fit the temperature dependencies of T_m:

$$\frac{1}{T_m} = \frac{1}{2T_1} + A_{SD,e} \frac{1}{\sqrt{T_1}} + C \dots\dots\dots\dots\dots\dots\dots\dots\dots\dots\dots\dots\dots\dots\dots \text{eq. S1}$$

where the first term describes the decoherence caused directly by spin relaxation, the second term describes the relaxation-induced electron spin diffusion (also called electronic spectral diffusion (SD)), and the constant term, C, encompasses three temperature-independent decoherence processes: nuclear spin diffusion (also called nuclear spectral diffusion), electron spin flip-flop, and instantaneous diffusion (ID). Note that the second term is different from Wilson's model in which the corresponding decoherence rate is inversely proportional to the T_1. Wilson et al. only considered the relaxation of nearby electron spins, but did not include the situation where a distant electron spin relaxes and then the spin flipping propagates to the interested electron spin, namely electronic SD. To correct this problem, we adopt a model considering the electronic SD,[8] which dictates that the decoherence rate is inversely proportional to the square root of T_1.

The temperature dependencies of T_m in the high-temperature region can be well fitted by the Equation S1 for both MgHOTP and TiHOTP. It turns out that for each material, the electronic SD causes the sharp decrease of T_m, and the constant term also significantly contributes to the decoherence. Therefore, although $1/2T_1$ is negligible, the T_m is indirectly limited by T_1 in the high-temperature region due to the electronic SD. We then extrapolated the above fitting results to the low- and medium-temperature regions and subtracted them from the $1/T_m$ of MgHOTP and TiHOTP (Supplementary Figure 9). The constant term is dominant in these temperature regions, indicating that nuclear SD, electron spin flip-flop, and/or ID play major roles in spin decoherence. The residual decoherence rate in each material shows a peak-shape curve with the maximum value at the same temperature, 28 K. Such coincidence might indicate similar origins of the motions.

The thermally activated behavior of the residual decoherence rate is similar to what was observed for the motion-induced decoherence process, where a slow motion at low temperature expedites the decoherence but a fast motion at high temperature improves coherence, the latter of which is called motional narrowing[9]. The motion may involve the methyl tunneling within $(CH_3)_2NH_2^+$ in TiHOTP and proton tunneling within hydrogen bonds in both MQFs (the O−H···O bond between coordinating H_2O and HOTP in MgHOTP and the N−H···O bond between $(CH_3)_2NH_2^+$ and HOTP in TiHOTP). Because methyl and proton tunneling rates typically show complex temperature dependencies

and are highly dependent on the molecular structure,[10–12] we cannot derive equations for these motions to fit their contributions to the decoherence. The exact origins of motions and the associated decoherence mechanisms in MgHOTP and TiHOTP are beyond the scope of this work and will be examined in the future.
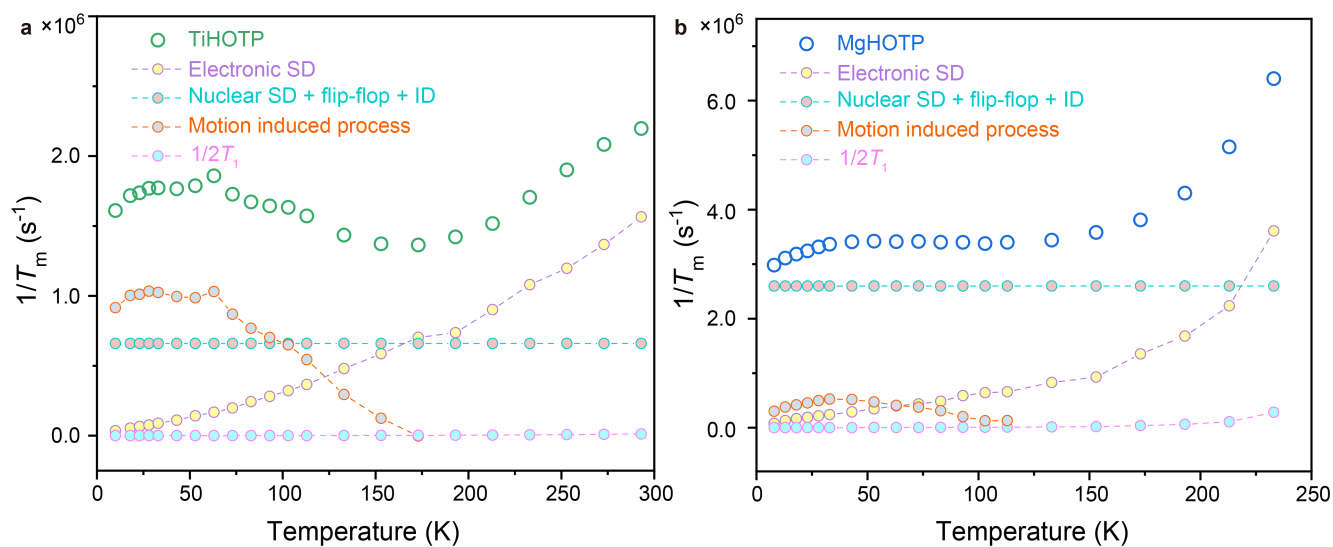
Supplementary Figure 9. Simulation of temperature dependencies of $1/T_m$ for a, TiHOTP and b, MgHOTP. Circles represent experimental data. Dotted dash lines represent contributions from various spin decoherence processes.

Supplementary Table 5. T_1 of selected metal-based molecular electron spin qubits.

Spin qubit[b]	T_1 / μs	Temperature/K	Frequency	Reference
VOPc:TiOPc = 1:1000	10000[a]	5[a]	X band	13
	1[a]	300[a]		
(PPh$_4$)$_2$[Cu(mnt)$_2$]$_{0.001\%}$	100000[a]	7[a]	Q band	14
	1[a]	300[a]		
(Ph$_4$P)$_2$[V(C$_8$S$_8$)$_3$]	36141[a]	10[a]	X-band	15
(Ph$_4$P)$_2$[V(β-C$_3$S$_5$)$_3$]	23237[a]			
(Ph$_4$P)$_2$[V(α-C$_3$S$_5$)$_3$]	16825[a]			
(Ph$_4$P)$_2$[V(C$_3$S$_4$O)$_3$]	17539[a]			
[VO(H$_2$O)$_5$]$^{2+}$	1000[a]	20[a]	Q band	16
[VO(nta)(H$_2$O)]$^-$	200[a]			
[VO(Hdtpa)]$^{2-}$	1000[a]			
[VO(ox)$_2$(H$_2$O)]$^{2-}$	2000[a]			
[VO(acac)$_2$(H$_2$O)]	30[a]			
Cu(acacen)$_{1\%}$	14000	5	X-band	17
	0.27	260		
[Ni(phen)$_3$](BF$_4$)$_2$	10[a]	5[a]	W-band	18
[Ni(pyr$_3$)$_2$](BF$_4$)$_2$	10[a]	5[a]		
[Cr(2,4-dimethylphenyl)$_4$]$_{1\%}$	400[a]	5[a]	X-band	19
[Cr(o-tolyl)$_4$]$_{1\%}$	5000[a]	5[a]		
[Cr(2,3-dimethylphenyl)$_4$]$_{1\%}$	2000[a]	5[a]		
[Cr(2,2,2-triphenylethyl)$_4$]$_{1\%}$	1000[a]	5[a]		
[Cr((trimethylsilyl)methyl)$_4$]$_{1\%}$	2000[a]	8[a]		
[Cr(cyclohexyl)$_4$]$_{1\%}$	3000[a]	5[a]		

[a]value estimated from a figure in the reference.

[b]VOPc = vanadyl phthalocyanine; TiOPc = titanyl phthalocyanine; mnt = 1,2-dicyanoethylene-1,2-dithiolate; Ph = phenyl;

nta = nitrilotriacetate; ox = oxalate; dtpa = diethylenetriaminepentaacetate; acac = acetylacetonato; acacen =

bis(acetylacetone)ethylenediamine; phen = 1,10-phenanthroline; pyr$_3$ = tris-2-pyridyl-methane.

7. Raman spectroscopy

A laser wavelength selection experiment was first performed. We tested 473 nm, 532 nm, and 633 nm, and 785 nm laser excitations. Under 473 nm and 532 nm laser conditions, the peak at 166 cm^{-1} becomes invisible, and peaks in the 1150 − 1700 cm^{-1} range become blurred and difficult to distinguish (Supplementary Figure 10). With a 785 nm laser, the signal from MgHOTP is extremely weak, making it challenging to obtain any meaningful data. For TiHOTP, although the signal is slightly stronger than that of MgHOTP, similar issues occur. Under 473 nm and 532 nm laser conditions, the peak ·centered at 700 cm^{-1} is weak, and the peaks in the 1150 − 1700 cm^{-1} range overlap significantly, making it difficult to extract valuable information. Based on these observations, we chose the 633 nm excitation wavelength for Raman spectroscopic measurements.
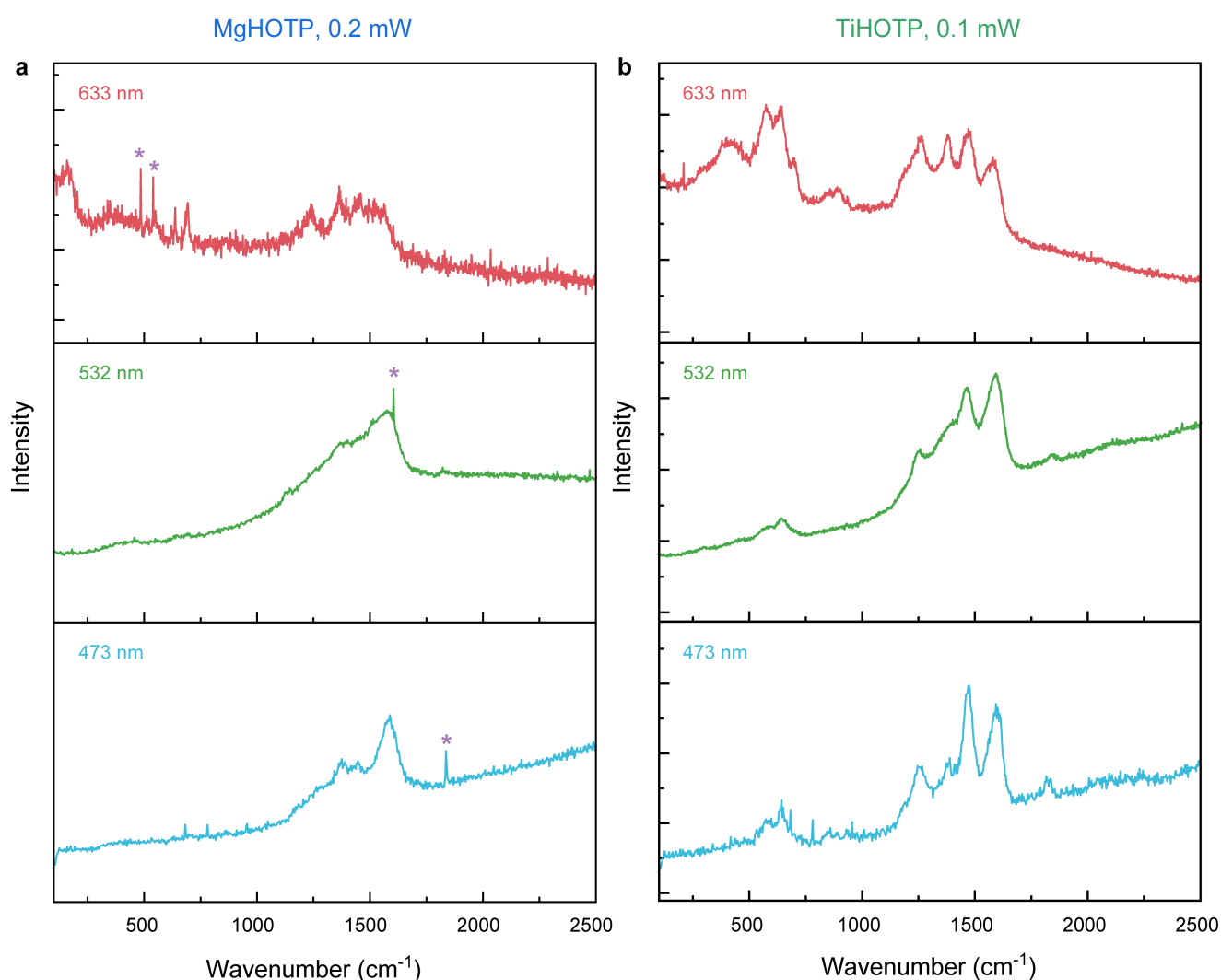
Supplementary Figure 10. Raman spectra of a, MgHOTP and b, TiHOTP acquired with different laser wavelengths and 0.2 mW for MgHOTP and 0.1 mW for TiHOTP laser power at 295K without magnetic field. The laser wavelength is indicated in each sub-plot. Peaks marked by asteroids are caused by cosmic rays.
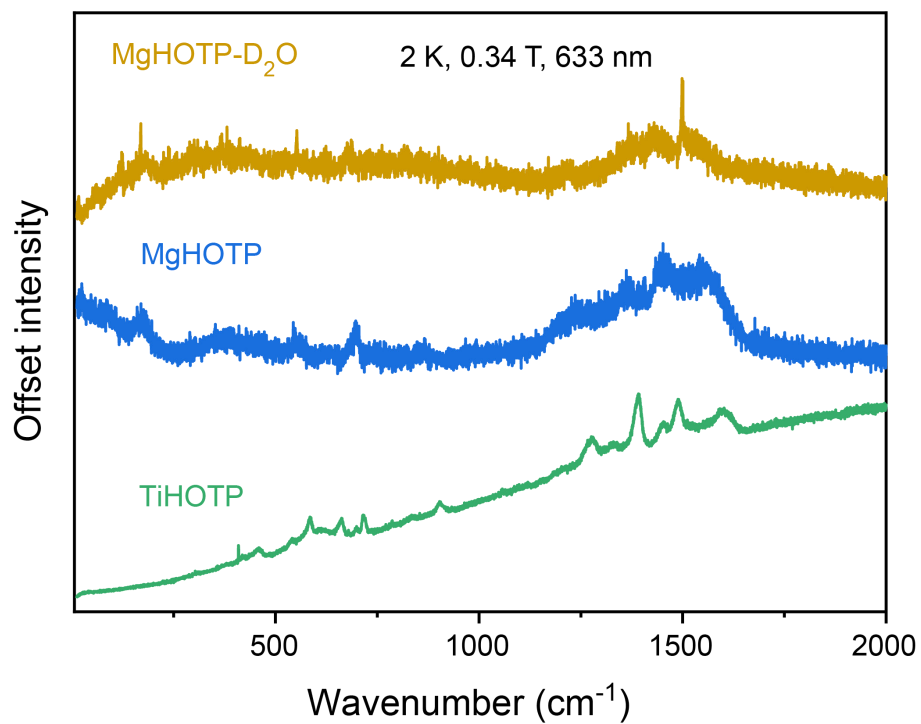
Supplementary Figure 11. Raman spectra of MgHOTP, TiHOTP, and MgHOTP-D₂O collected at 2 K and 0.34 T under 633 nm excitation.
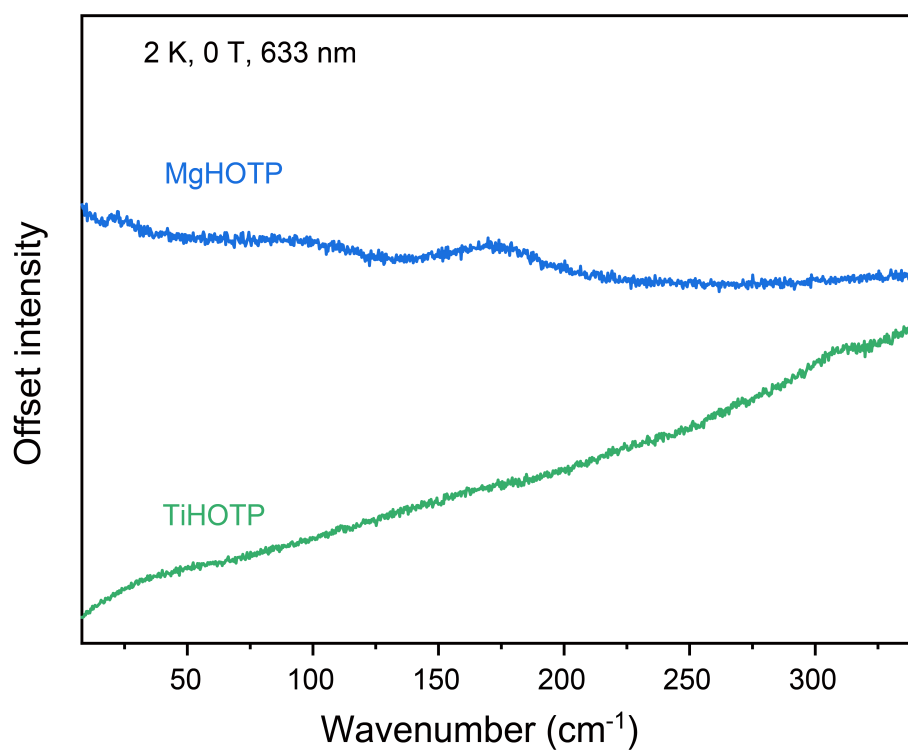
Supplementary Figure 12. Raman spectra of MgHOTP and TiHOTP collected at 2 K and 0 T under 633 nm excitation.
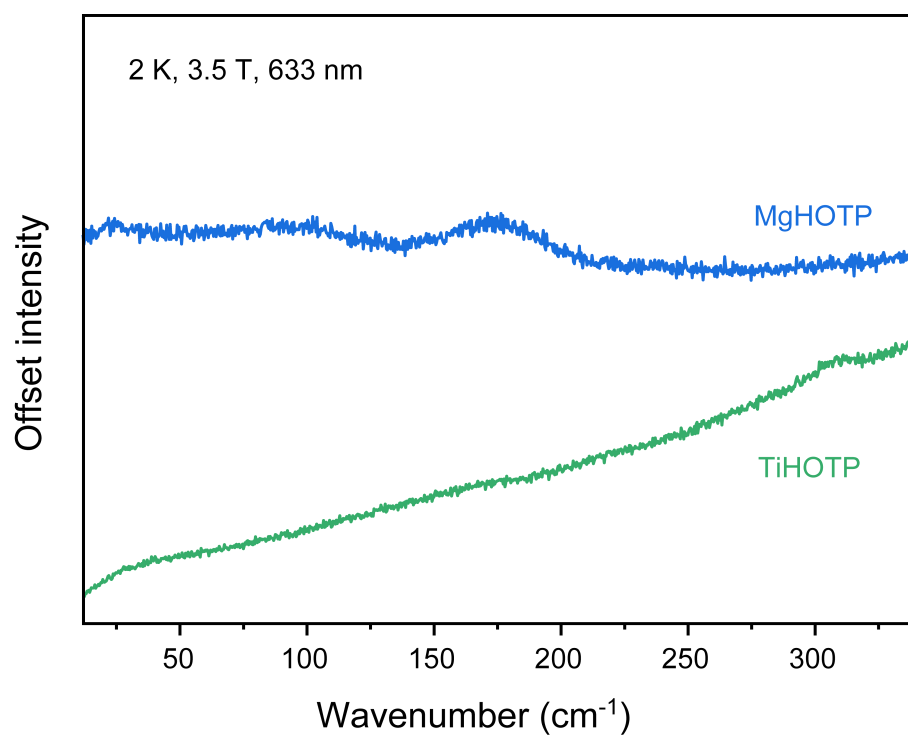
Supplementary Figure 13. Raman spectra of MgHOTP and TiHOTP collected at 2 K and 3.5 T under 633 nm excitation.

8. Brillouin light scattering spectroscopy

In our BLS results as shown in Supplementary Figure 14−16, TiHOTP, MgHOTP, and MgHOTP-D2O display no phonon features in the frequency range of 3 GHz − 300 GHz (0.1 cm^{-1} − 10 cm^{-1}). In Supplementary Figure 14 and 15, the low-frequency region of the spectra exhibits significant Rayleigh broadening, which originates from elastic scattering due to entropy fluctuation in the materials. Generally, the more complex the system contributes the larger the linewidth of the Rayleigh scattering. In Supplementary Figure 15, the sharp peaks near the 33 GHz in the BLS spectra of MOFs and Si have been observed in a variety of systems and originate from the instruments.[20] The absence of a phonon signal measured by the BLS implies that the acoustic vibrations are weak in strength and contribute negligibly to the Debye temperature, so it is reasonable to consider only optical phonons.
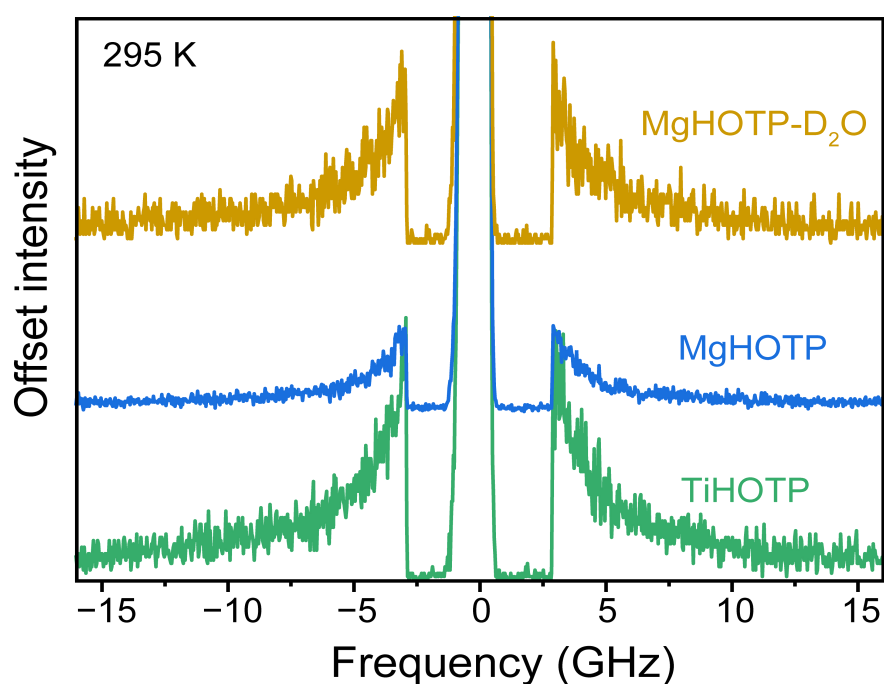
Supplementary Figure 14. Brillouin light scattering spectra of MgHOTP, TiHOTP, and MgHOTP-D$_2$O in the frequency range of 3 − 16 GHz at 295 K.
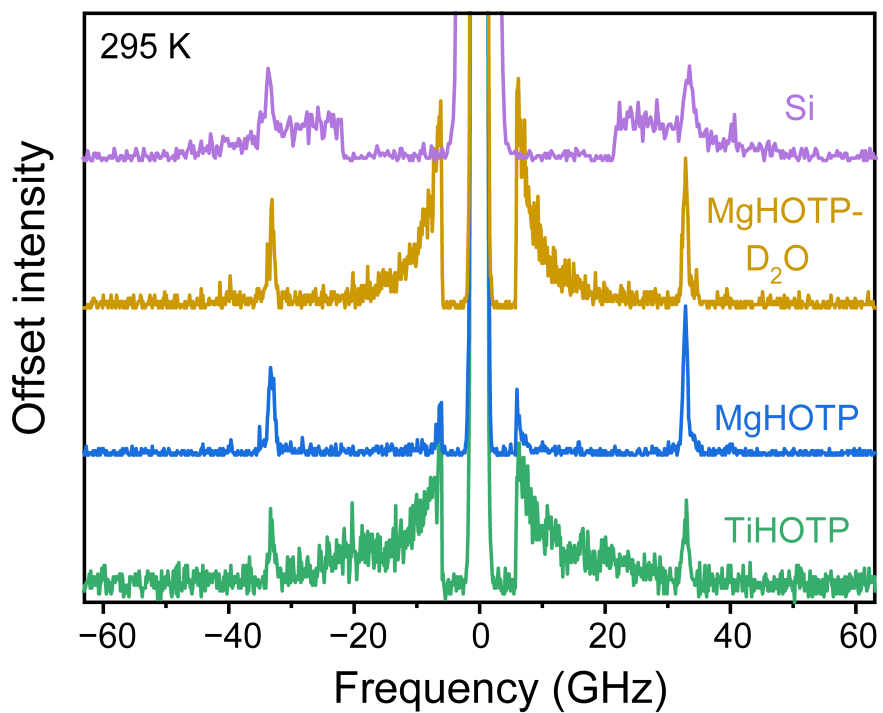
Supplementary Figure 15. Brillouin light scattering spectra of MgHOTP, TiHOTP, and MgHOTP-D$_2$O, and Si substate in the frequency range of 16 − 60 GHz at 295 K. The peak at 33 GHz stems from background noise of the instrument.
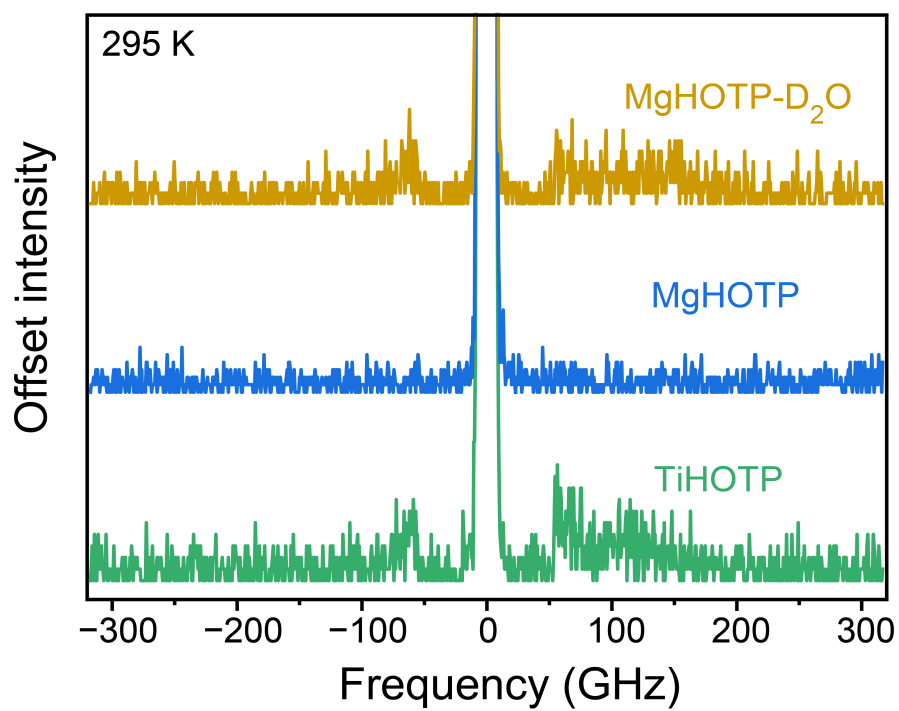
Supplementary Figure 16. Brillouin light scattering spectra of MgHOTP, TiHOTP, and MgHOTP-D$_2$O in the frequency range of 60 − 300 GHz at 295 K.

9. DFT Calculation of vibration mode
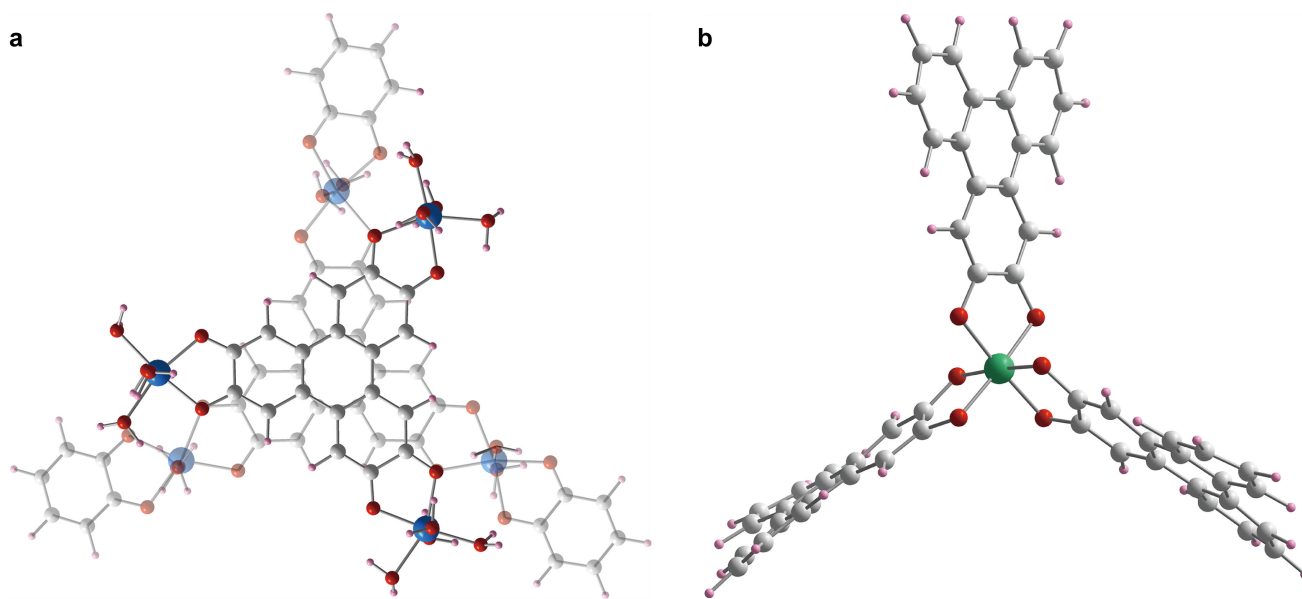
Supplementary Figure 17. A portion of a, MgHOTP and b, TiHOTP used for calculation.
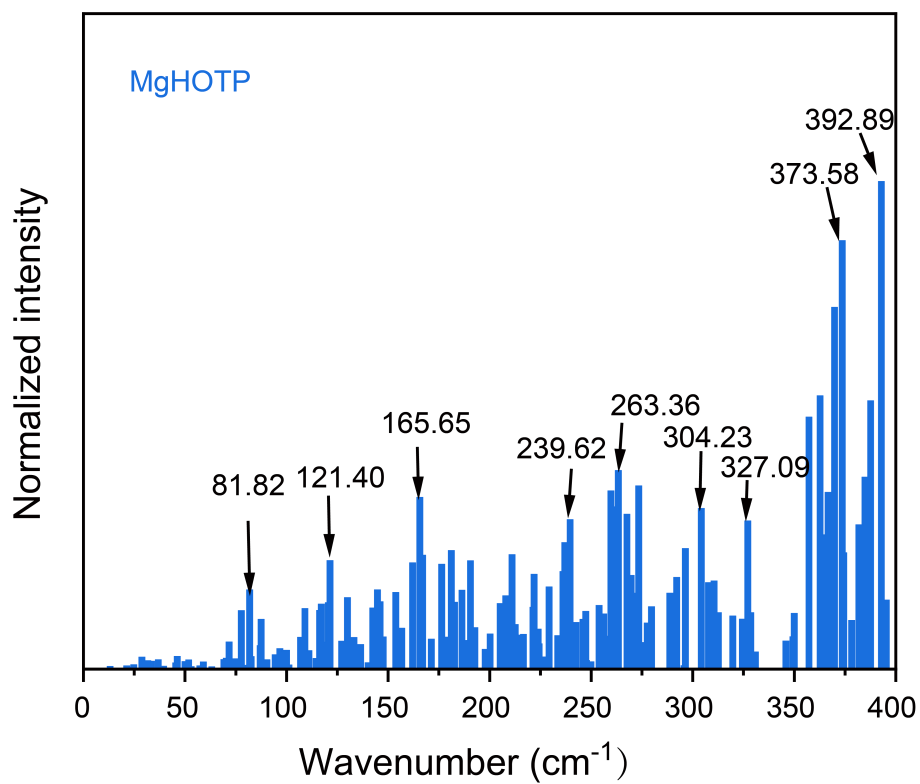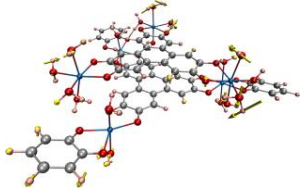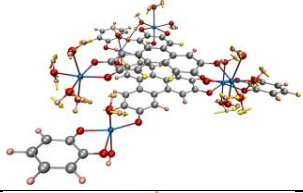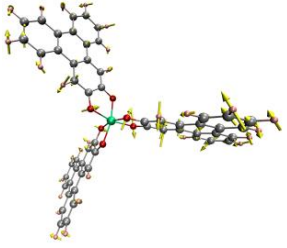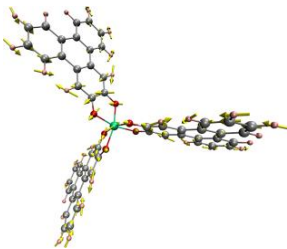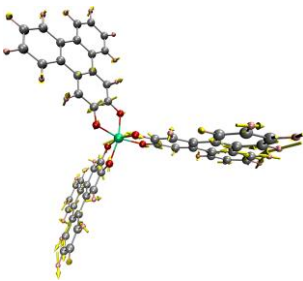
Supplementary Figure 18. Vibration modes of MgHOTP.
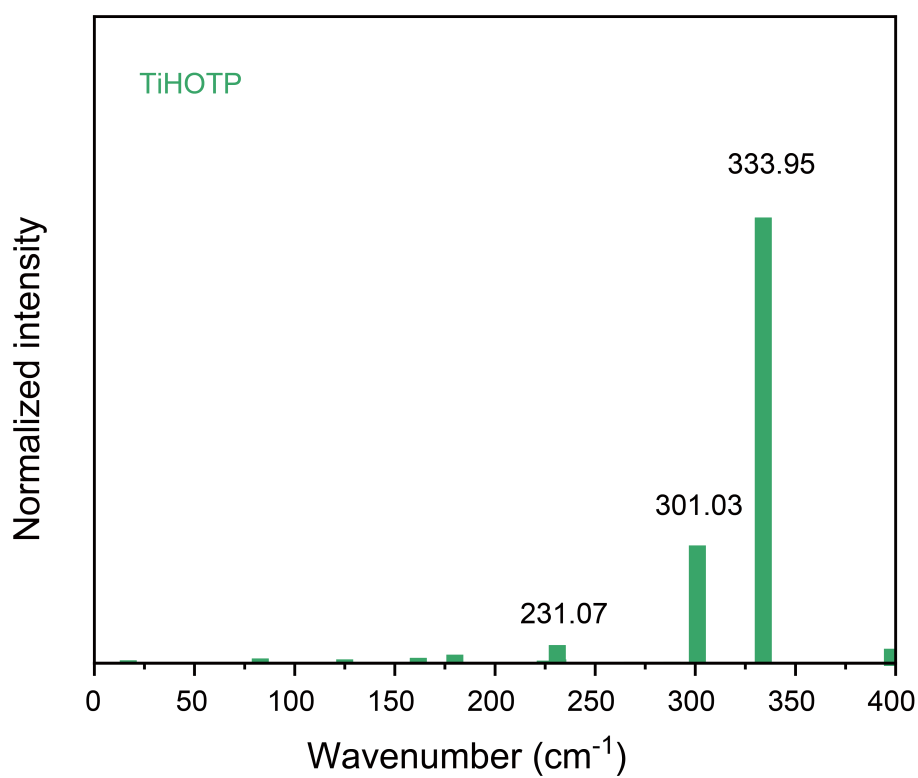
Supplementary Figure 19. Vibration modes of TiHOTP.

Supplementary Table 6. Schematic representation of vibration modes of MgHOTP and TiHOTP. The arrow represents the direction of atomic displacement.

MQF	Wavenumber (cm^{-1})	Vibration mode
MgHOTP	81.82	
	121.40	
	165.65	
TiHOTP	231.07	
	301.03	
	333.95	

Supplementary Table 7. Calculated normal modes in the MgHOTP fragment.

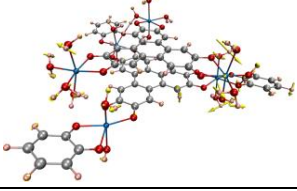| Freq.[a] (cm⁻¹)	eps[a] (L·mol⁻¹·cm⁻¹)	Freq.[a] (cm⁻¹)	eps[a] (L·mol⁻¹·cm⁻¹)	Freq.[a] (cm⁻¹)	eps[a] (L·mol⁻¹·cm⁻¹)	Freq.[a] (cm⁻¹)	eps[a] (L·mol⁻¹·cm⁻¹)
4.94	0	109.06	0.00497	212.62	0.003662	307.8	0.007086
13.13	0.000264	111	0.001545	215.48	0.002801	310.5	0.007214
21.27	0.000306	114.55	0.000907	216.65	0.00287	312.64	0.004628
22.12	0.000194	116.32	0.004813	221.3	0.005074	319.69	0.004368
24.77	0.000388	117.09	0.005329	221.85	0.007762	324.41	0.004111
25.98	0.00001	119.91	0.002239	223.92	0.003291	327.09	0.012104
28.79	0.001005	120.6	0.005442	224.4	0.0021	328.54	0.004632
31.66	0.000726	121.4	0.008868	226.73	0.000702	330.88	0.001434
33.54	0.000686	127.13	0.002309	227.12	0.001022	345.89	0.002318
36.84	0.000797	129.96	0.005852	229.26	0.006735	349.3	0.002674
39.43	0.000272	130.56	0.00217	233.52	0.002757	350.01	0.004575
45.42	0.000539	133.15	0.002609	236.13	0.007983		
46.17	0.001065	136.42	0.002042	237	0.010343		
49.99	0.000644	140.14	0.000557	237.9	0.004838		
51.78	0.000778	142.43	0.005011	239.62	0.012214		
53.01	0.000237	144.73	0.006491	242.52	0.003838		
56.48	0.000111	146.07	0.005523	245.98	0.004092		
57.26	0.000296	147.57	0.002661	247.35	0.004738		
59.07	0.000611	153.78	0.006284	247.7	0.000732		
63.18	0.00022	156.67	0.003371	249.87	0.000638		
67.29	0.000039	162.06	0.008692	253.87	0.005222		
69.12	0.000812	165.65	0.014016	256.2	0.004526		
70.34	0.000922	167.05	0.009317	257.47	0.002721		
71.68	0.002255	171.29	0.002469	259.73	0.014544		
74.94	0.000875	176.4	0.008569	262.04	0.013252		
77.73	0.004795	178.45	0.002638	263.36	0.016214		
78.79	0.000351	181.1	0.009695	267.6	0.012643		
81.82	0.006489	182.65	0.005475	269.63	0.007667		
82.56	0.001053	186.37	0.006465	272.24	0.006224		
87.05	0.001941	187.76	0.002375	273.39	0.014952		
87.5	0.004095	190.57	0.008865	275.53	0.002201		
90.32	0.000795	192.76	0.003415	277.57	0.00379		
94.41	0.001209	197.82	0.001648	279.71	0.005122		
96.71	0.001705	200.23	0.002899	288.71	0.006216		
98.63	0.000541	205.23	0.005374	292.11	0.007501		
100.01	0.001567	207.88	0.00601	295.73	0.000313		
101.22	0.000381	208.53	0.005274	296.36	0.009856		
106.87	0.002622	211.05	0.009356	304.23	0.013113		

[a]Freq.: Frequency; eps: epsilon, i.e. molar absorption coefficient.

Supplementary Table 8. Calculated normal modes in the TiHOTP fragment.

Freq. [a] (cm^{-1})	eps [a] (L·mol^{-1}·cm^{-1})	Freq. [a] (cm^{-1})	eps (L·mol^{-1}·cm^{-1})
6.58	0.00002	301.03	0.003974
6.58	0.00002	333.94	0.015042
12.19	0	333.95	0.015042
12.4	0.000001	398.44	0.000487
12.4	0.000001	407.1	0.000686
16.94	0.000099		
45.42	0.000026		
46.25	0		
46.25	0		
62.62	0.000025		
62.62	0.000025		
67.65	0		
73.9	0.000019		
82.83	0.000162		
82.83	0.000162		
100.88	0.000029		
100.88	0.000029		
107.52	0.000032		
107.52	0.000032		
115.28	0		
122.49	0		
124.96	0.000127		
161.74	0.000183		
161.74	0.000183		
179.96	0.00029		
225.09	0.000085		
225.09	0.000085		
231.06	0.000613		
231.07	0.000613		
231.37	0.000131		
237.88	0		
263.86	0.000016		
263.86	0.000016		
269.17	0.000002		
269.17	0.000002		
272.94	0		
288.36	0.000049		
288.37	0.00005		
289.87	0		

[a]Freq.: Frequency; eps: epsilon, i.e. molar absorption coefficient.

10. W-band pulse EPR spectroscopy

The T_1 of MgHOTP and TiHOTP was measured by the inversion recovery pulse sequence with W-band pulse EPR spectroscopy (samples of different synthetic batches were used for X-band and W-band pulse EPR measurements). The experimental parameters and data analysis methods were the same with those described for X-band pulse EPR spectroscopy except for π pulse lengths. For MgHOTP, the π pulse length was 120 ns, whereas the π pulse length for TiHOTP varies between 48 and 120 ns due to limitations of the instrument.
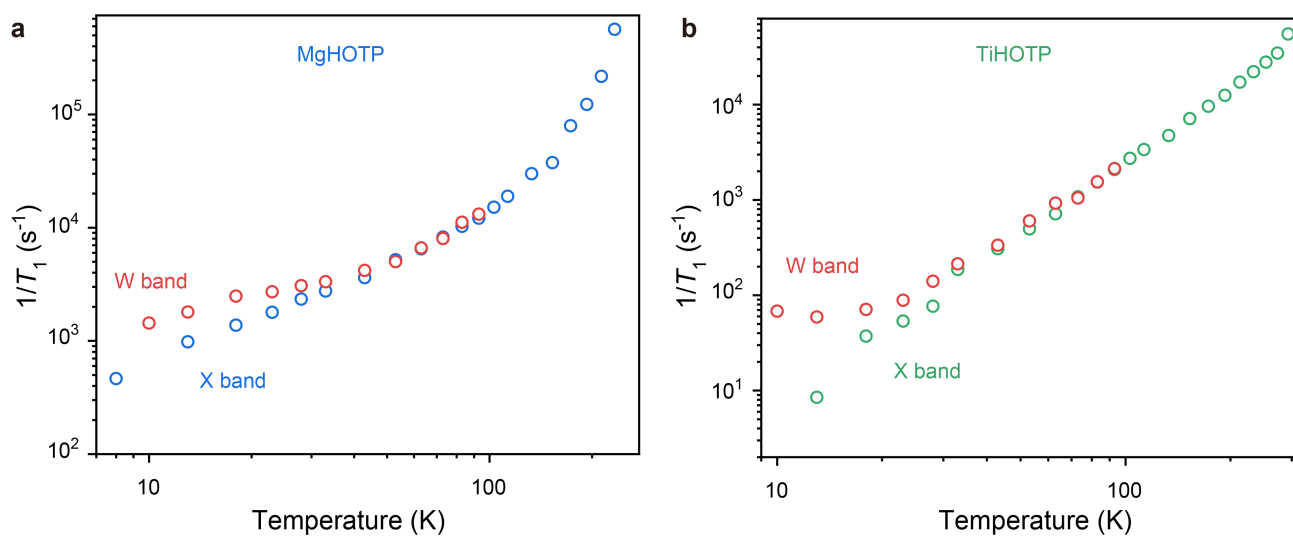
Supplementary Figure 20. Variable-temperature T_1 of a, MgHOTP and b, TiHOTP acquired at X-band and W-band.

Supplementary Table 9. T_1 of MgHOTP at various temperatures acquired at X-band and W-band.

Temperature (K)	T_1 (µs), W-band	T_s (µs), W-band	T_1 (µs), X-band	T_s (µs), X-band
10	6.9 (2) × 10^2	5.6 (2) × 10^1		
13	5.6 (1) × 10^2	5.2 (1) × 10^2	1.32 (2) × 10^3	3.84 (8) × 10^3
18	4.09 (8) × 10^2	4.16 (8) × 10^2	8.4 (1) × 10^2	2.27 (5) × 10^2
23	3.69 (7) × 10^2	4.24 (9) × 10^2	6.5 (1) × 10^2	1.77 (4) × 10^2
28	3.29 (6) × 10^2	4.02 (8) × 10^1	4.83 (7) × 10^2	1.37 (3) × 10^2
33	3.00 (6) × 10^2	3.93 (8) × 10^1	3.99 (5) × 10^2	1.10 (2) × 10^2
43	2.39 (5) × 10^2	3.44(7) × 10^1	2.76 (4) × 10^2	6.63 (2) × 10^1
53	1.95 (4) × 10^2	3.01 (6) × 10^1	1.92 (3) × 10^2	4.6 (1) × 10^1
63	1.51 (3) × 10^2	2.55 (5) × 10^1	1.44 (2) × 10^2	3.5 (1) × 10^1
73	1.25 (3) × 10^2	2.25 4) × 10^1	1.21 (3) × 10^2	3.3 (1) × 10^1
83	8.7 (1) × 10^1	1.77 (3) × 10^1	9.7 (3) × 10^1	2.7 (1) × 10^1
93	7.6 (2) × 10^1	1.58 (4) × 10^1	6.7 (1) × 10^1	1.76 (7) × 10^1

Supplementary Table 10. T_1 of TiHOTP at various temperatures acquired at X-band and W-band.

Temperature (K)	T_1 (µs), W-band	T_s (µs), W-band	T_1 (µs), X-band	T_s (µs), X-band
10	1.6 (1) × 10^4	8.6 (4) × 10^3		
13	1.69 (7) × 10^4	1.78 (3) × 10^3	9.1 (3) × 10^4	1.03 (1) × 10^4
18	1.36 (6) × 10^4	1.76 (5) × 10^3	2.19 (5) × 10^4	5.46 (8) × 10^3
23	1.13 (4) × 10^4	1.68 (8) × 10^3	1.49 (3) × 10^4	4.02 (7) × 10^3
28	7.2 (2) × 10^3	1.50 (8) × 10^3	1.04 (2) × 10^4	2.97 (5) × 10^3
33	4.7 (1) × 10^3	1.11 (5) × 10^3	5.37 (7) × 10^3	9.2 (3) × 10^2
43	3.0 (1) × 10^3	8.3 (4) × 10^2	3.25 (4) × 10^3	6.0 (2) × 10^2
53	1.63 (6) × 10^3	5.4 (2) × 10^2	2.01 (2) × 10^3	3.9 (1) × 10^2
63	1.48 (2) × 10^3	4.9 (2) × 10^2	1.40 (2) × 10^3	2.88 (9) × 10^2
73	9.7 (1) × 10^2	3.7 (2) × 10^2	9.3 (1) × 10^2	1.93 (6) × 10^2
83	6.46 (9) × 10^2	2.6 (1) × 10^2	7.17 (6) × 10^2	2.06(4) × 10^2
93	4.76 (7) × 10^2	2.6 (2) × 10^2	4.80 (4) × 10^2	1.03 (3) × 10^2

11. Mechanistic analysis of spin-lattice relaxation at X-band (Supplementary Note 11)

(1) Initial trials on the fitting of $1/T_1$ vs. T data

As discussed in the main text, the spin-lattice relaxation in both MgHOTP and TiHOTP is governed by the direct process at low temperatures and the two-phonon processes at high temperatures. Accordingly, we tried the following equation to fit temperature dependencies of T_1:

$$\frac{1}{T_1} = A_{Dir}T + A_{two-phonon}T^m \dots\dots\dots\dots\dots\dots\dots\dots\dots\dots\dots\dots\dots\dots\text{ eq. S2}$$

where A_{Dir} and $A_{two-phonon}$ represent pre-factors that describe contributions of the direct and two-phonon processes, respectively, m is an exponential factor, and T represents the temperature. This equation fits the $1/T_1$ vs. T relationship well (Supplementary Figure 21).
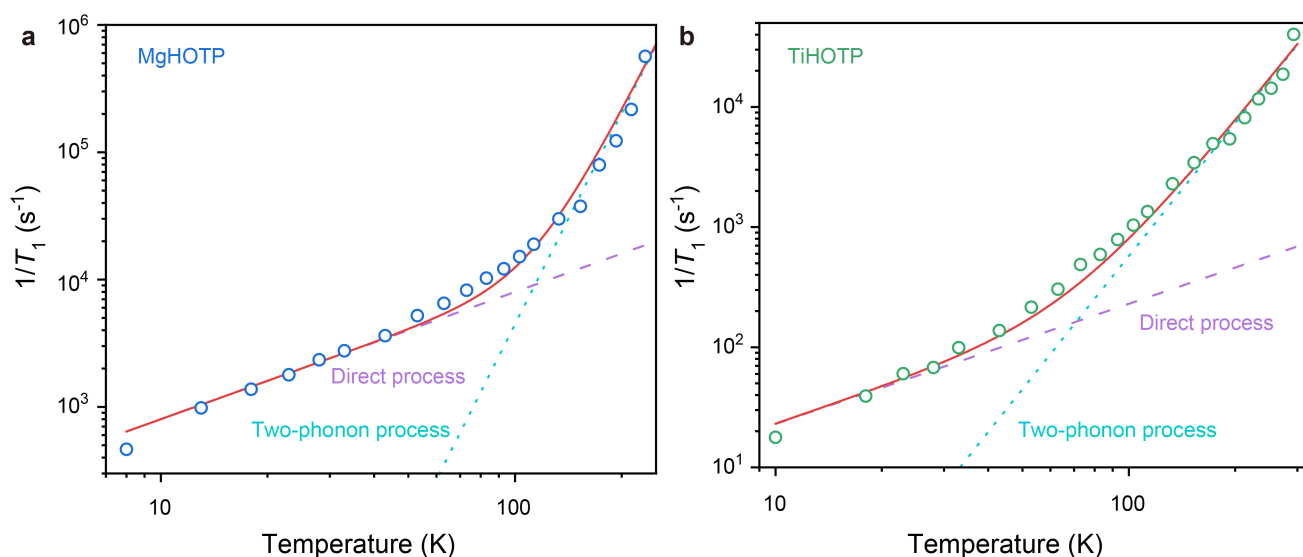
Supplementary Figure 21. Simulations of T_1 values acquired at various temperatures and X-band for a, MgHOTP and b, TiHOTP. Circles represent experimental data. Purple dash lines and light blue dot lines represent contributions from direct and two-phonon relaxation processes, respectively, and red lines represent their sum.

Although the second term has been widely used to describe the two-phonon relaxation of molecular magnets and electron spin qubits,[21–25] its physical meaning is unclear and under debate. Shrivastava claimed that m can take any value between 2 and 9 depending on experimental conditions and sample properties,[26] whereas Gu et al. argued that such power-law relaxation may be a manifestation of the combination of direct process and many local-mode processes.[27] As the power-law relationship does not inform details regarding the phonons that participate in the spin-lattice relaxation, we tend to divide it into an acoustic phonon term (Raman process based on the Debye model) and multiple optical phonon terms (local-mode processes). Further, methyl tunneling and proton tunneling in MgHOTP and TiHOTP may cause thermally activated relaxation. Putting together, we considered the following four relaxation processes:[28]

Direct process: $\frac{1}{T_{1,Dir}} = A_{Dir}T$ ....eq. S3

Raman process: $\frac{1}{T_{1,Ram}} = A_{Ram}\left(\frac{T}{T_D}\right)^9 \int_0^{\frac{T_D}{T}} x^8 \frac{e^x}{(e^x-1)^2}\, dx$ ....eq. S4

Local-mode process: $\frac{1}{T_{1,Loc}} = A_{Loc}\frac{e^{h\nu/k_BT}}{\left(e^{h\nu/k_BT}-1\right)^2}$ .... eq. S5

Thermally activated process: $\frac{1}{T_{1,Therm}} = A_{Therm}\frac{2\tau_{c,0}e^{Ea/k_BT}}{1+\omega^2\tau_{c,0}{}^2 e^{Ea/k_BT}}$ .... eq. S6

where T_D the Debye temperature, h the Planck constant, k_B the Boltzmann constant, ν the linear frequency of the optical phonon participating in the local-mode process, ω the Larmor frequency of electron spin, $\tau_{c,0}$ the pre-exponential factor of the correlation time of the thermally activated process, E_a the activation energy. The left side of each equation is the relaxation rate of each process, and A_{Dir}, A_{Ram}, A_{Loc}, A_{Therm} are pre-factors.

We found that the fitting of $1/T_1$ vs. T relationship with the abovementioned four processes is unfeasible for MgHOTP and TiHOTP. First, the $1/T_1$ data span several orders of magnitude. As data points with larger $1/T_1$ values introduce larger absolute errors, the fitting tends to minimize the errors for these data points by compromising the accuracy for the data points with smaller $1/T_1$ values. Second, the high-level nonlinearity of Equation S3−6 makes the fitting parameters relatively dependent on each other. Third, it is difficult to decide a priori how many local-mode processes should be involved in the fitting. Therefore, it is not straightforward to fit the $1/T_1$ vs. T data directly.

(2) Simulation of $1/T_1$ vs T data for TiHOTP

We tried various combinations of the abovementioned four processes to simulate the $1/T_1$ vs T relationship to search for the best matches with experimental data. The T_D was constrained to be below its upper limit (35 K for MgHOTP, 22 K for MgHOTP-D$_2$O, and 446 K for TiHOTP). Optical phonon frequencies used for local-mode processes were extracted from vibrational spectroscopy. Specifically, we chose optical phonons corresponding to C−O stretches, metal−oxygen stretches, as well as low-frequency modes of hydrogen-bonded networks. These optical phonons are most likely responsible for local-mode processes as they involve the oxygen atoms of the HOTP radical on which electron spins mainly reside. Considering the Occam's razor principle, we chose minimum number of relaxation processes for the simulation.

We first analyzed thermal behaviors of the Raman process and the local-mode process. Given constant pre-factors, the Raman relaxation rate increases with increasing T_D and rising temperature (Supplementary Fig. 22c), and the local-mode relaxation rate increases with increasing optical phonon frequency and rising temperature. At the high-temperature limit where T ≫ T_D or T ≫ $h\nu/k_B$, the rate of Raman process or local-mode process scales with T^2. For instance, as shown in Supplementary Fig. 22a, this scaling holds true for the Raman process with T > T_D = 10 K; it is also applicable to the local-mode process with ν/c = 24 cm^{-1} and T > 35 K (or ν/c = 15 cm^{-1} and T > 22 K; c represents the speed of light). The scaling of Raman process is above 2 when T < T_D (Supplementary Fig. 22b).

30

With this knowledge, we simulated the temperature dependence of $1/T_1$ for TiHOTP. Various combinations of the abovementioned four relaxation processes were tested. Four optical phonon frequencies, including 310 cm^{-1}, 714 cm^{-1}, 1391 cm^{-1}, and 1489 cm^{-1}, were considered for the local-mode process, which correspond to Ti−O stretch coupled with a scissoring mode of HOTP, Ti−O stretch itself, C−O stretch in the deprotonated catechol moiety, and C−O stretch in the semiquinone moiety, respectively. The best simulation was found by combining the direct process, Raman process with T_D = 263 K, and a local-mode process with v/c = 1489 cm^{-1} (Supplementary Figure 23b). Replacing the local-mode process by one with v/c = 714 cm^{-1} generates comparable results (Supplementary Figure 24b). Both optical phonons may participate in local-mode processes, which is reasonable because Ti−O stretch and C−O stretch in the semiquinone moiety directly influences the electron spin residing on the oxygen atoms of HOTP. Notably, replacing the local-mode process by one with v/c = 310 cm^{-1} or v/c = 1391 cm^{-1} do not give rise to comparable match (Supplementary Figure 24a, c).

We conducted additional simulations to verify the optimality of the abovementioned spin-lattice relaxation mechanisms. First, we tried to use a low T_D (T_D = 10 K) such that the Raman process reaches the high-temperature limit in our experimental temperature (T ≥ 10 K). The combination of such Raman process and a local-mode process with v/c = 1489 cm^{-1} do not generate reasonable match (Supplementary Figure 24d). Second, we tried to replace the Raman process by a local-mode process with the lowest optical phonon frequency (v/c = 310 cm^{-1}), which is akin to the best simulation of MgHOTP (*vide infra*). Such simulation cannot reproduce the data below 53 K (Supplementary Figure 24e). These trials suggest that TiHOTP has a high T_D and that its relaxation at relatively high temperature is primarily governed by acoustic phonons and optical phonons arising from C−O and Ti−O bonds. Third, considering the pronounced motion narrowing effect observed in the spin decoherence (Supplementary Note 5), we also attempted to analyze the temperature dependence of T_1 using a thermally activated process (Supplementary Figure 24f). However, the thermally activated process involves three adjustable parameters and is highly nonlinear, so it tends to generate overfitting. Additionally, since the theory of the motion narrowing effect is not yet fully understood, simulation with the thermally activated process does not yield reliable information.
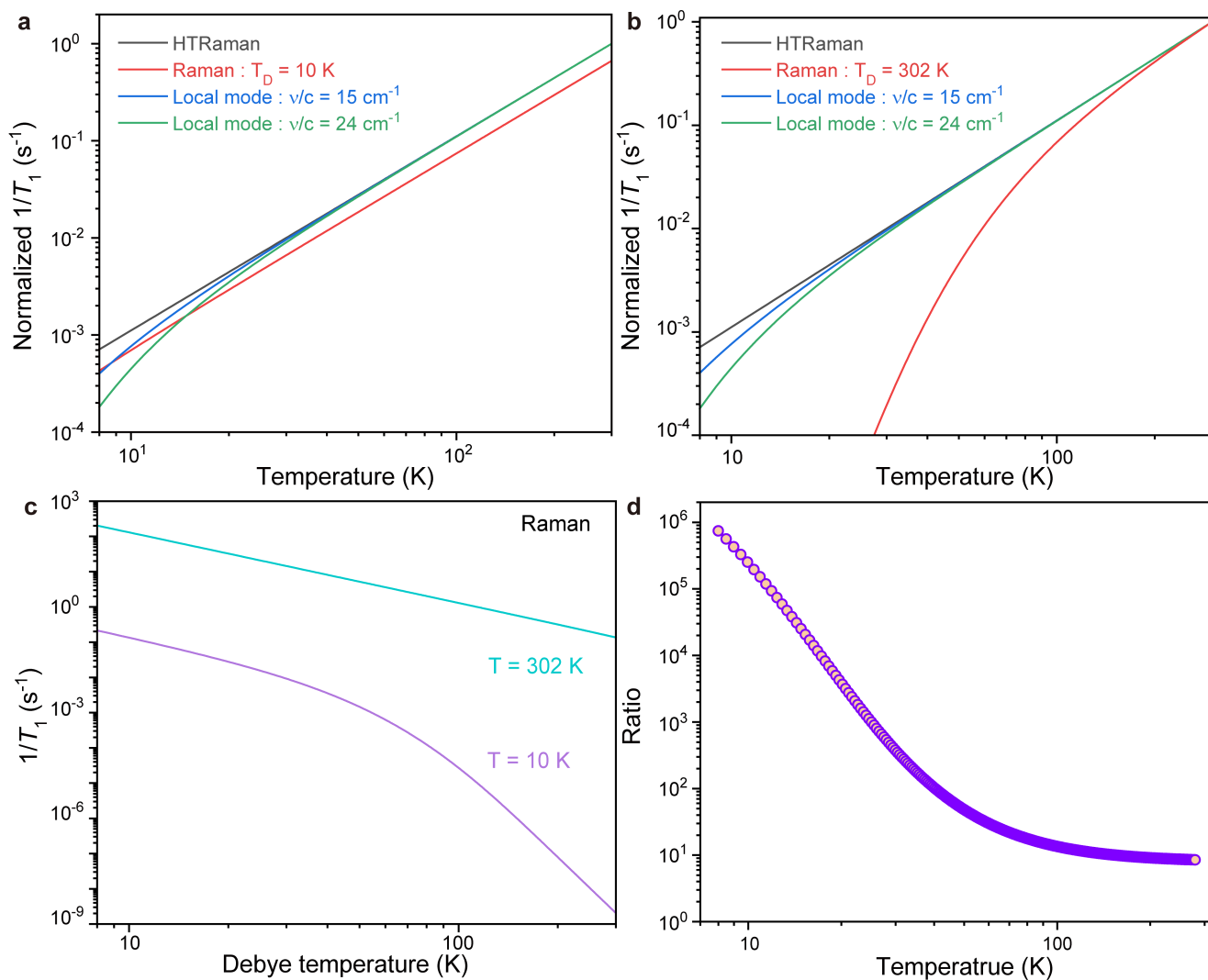
Supplementary Figure 22. a, Comparison of the Raman process at its high-temperature limit, the Raman process with T_D = 10 K, the local-mode process with v/c = 15 cm^{-1}, and the local-mode process with v/c = 24 cm^{-1}. b, Comparison of the Raman process at its high-temperature limit, the Raman process with T_D = 302 K, the local-mode process with v/c = 15 cm^{-1}, and the local-mode process with v/c = 24 cm^{-1}. c, T_D-dependencies of $1/T_1$ in the Raman process at T = 10 K and T = 302 K. d, ratio of the relaxation rates of the local-mode process with v/c = 24 cm^{-1} for MgHOTP and the Raman process with T_D = 302 K for TiHOTP.
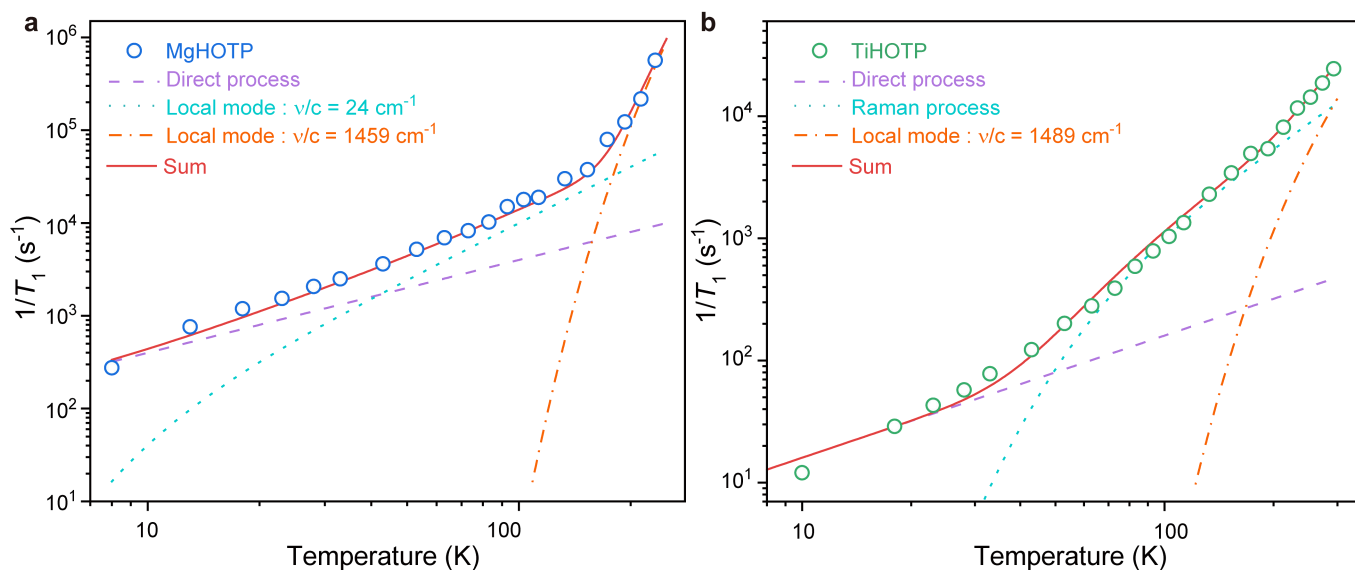
Supplementary Figure 23. Spin-lattice relaxation rates (1/T_1) of a, MgHOTP and b, TiHOTP acquired at various temperatures and their optimal simulation results. Circles represent experimental data. Purple dash lines represent contributions from direct processes. Light blue dot lines represent contributions from the local-mode process driven by the 24 cm^{-1} optical phonon for MgHOTP or the Raman process for TiHOTP. Orange dash-dot lines represent contributions from local-mode processes driven by C−O stretches in semiquinone moieties. Red solid lines represent the sum of all relaxation processes.
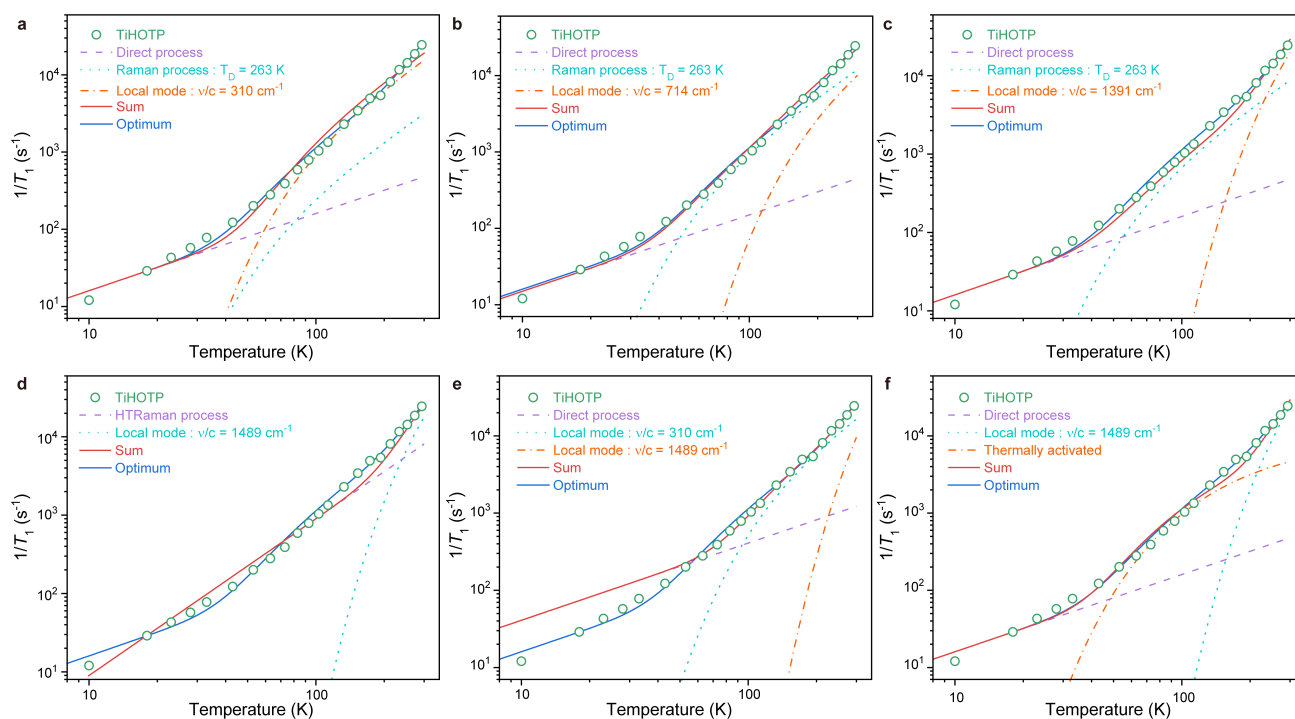
Supplementary Figure 24. Simulations of the temperature dependence of 1/T_1 for TiHOTP involving various spin-lattice relaxation processes. a, Direct process, Raman process, and a local-mode process with v/c = 310 cm^{-1}. b, Direct process, Raman process, and a local-mode process with v/c = 714 cm^{-1}. c, Direct process, Raman process,
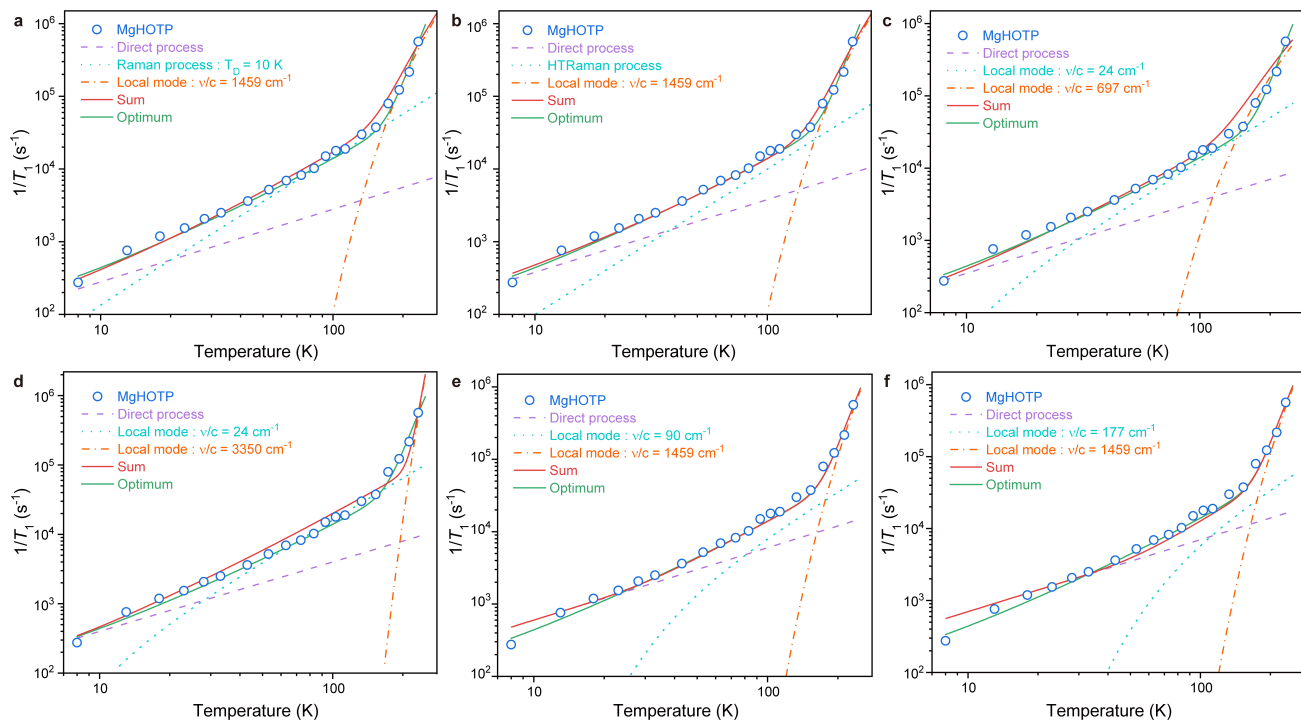
33

and a local-mode process with v/c = 1391 cm^{-1}. d, Raman process at its high-temperature limit (HTRaman) and a local mode with v/c = 310 cm^{-1}. e, Direct process, a local-mode process with v/c = 310 cm^{-1}, and another local-mode process with v/c = 1489 cm^{-1}. f, Direct process, a local-mode process with v/c = 1489 cm^{-1}, and a thermally activated process. The optimum involves the direct process, Raman process with T_D = 263 K, and a local-mode process with v/c = 1489 cm^{-1}; its simulation curve is shown in Fig. 4b.

(3) Simulation of 1/T_1 vs T data for MgHOTP

We simulated the temperature dependence of 1/T_1 for MgHOTP using a similar approach. Three low-frequency optical phonons (v/c = 24 cm^{-1}, 90 cm^{-1}, and 177 cm^{-1}) and three high-frequency ones (v/c = 697 cm^{-1}, 1459 cm^{-1}, and 3350 cm^{-1}) were tested for local-mode processes. The latter three correspond to the Mg−O stretch, C−O stretch in the semiquinone moiety, and O−H stretch in the coordinating H_2O. Note that the T_D is upper-bounded by 35 K and the lowest-frequency optical phonon is at 24 cm^{-1}. Thus, both the Raman process and the corresponding local-mode process reach their high-temperature limits above 40 K. Both may contribute to the spin-lattice relaxation and it is difficult to distinguish their contributions.

The simulation based on a combination of direct process and the local-mode process with v = 24 cm^{-1} closely reproduced the experimental data below 100 K (Supplementary Figure 23a). As expected, replacing the local-mode process with the Raman process with T_D = 10 K generates comparable results (Supplementary Figure 25a). The exact T_D cannot be determined, though, because the Raman process reaches its high-temperature limit in the experimental temperature range (T ≥ 8 K) (Supplementary Figure 25b). Nonetheless, replacing the local-mode process by one with v/c = 90 cm^{-1} or v/c = 177 cm^{-1} does not generate good matches below 33 K (Supplementary Figure 25e, f). The optical phonon at 24 cm^{-1} likely plays a major role in the spin-lattice relaxation.

The high-frequency optical phonons should be responsible for the upturn of 1/T_1 above 180 K. Simulations revealed that the local-mode process with v/c = 1459 cm^{-1} shows the best match with the experimental data, yet those with v/c = 697 cm^{-1} or v/c = 3350 cm^{-1} do not yield consistent trends (Supplementary Figure 25c, d). In summary, the optimal simulation stems from the combination of the direct process, a local-mode process driven by the optical phonon at 24 cm^{-1} (or the Raman process at the high-temperature limit), and another local-mode process driven by the optical phonon at 1459 cm^{-1}.

Supplementary Figure 25. Simulations of the temperature dependence of $1/T_1$ for MgHOTP involving various spin-lattice relaxation processes. a, Direct process, Raman process with $T_D = 10$ K, and a local-mode process with v/c = 310 cm^{-1}. b, Direct process, Raman process at its high-temperature limit (HTRaman), and a local-mode process with v/c = 1459 cm^{-1}. c, Direct process, a local-mode process with v/c =24 cm^{-1}, and another local-mode process with v/c = 697 cm^{-1}. d, Direct process, a local-mode process with v/c = 24 cm^{-1}, and another local-mode process with v/c = 3350 cm^{-1}. e, Direct process, a local-mode process with v/c = 90 cm^{-1}, and another local-mode process with v/c = 1459 cm^{-1}. f, Direct process, a local-mode process with v/c = 177 cm^{-1}, and another local-mode process with v/c = 310 cm^{-1}. The optimum involves the direct process, a local-mode process with v/c = 24 cm^{-1}, and another local-mode process with v/c = 1459 cm^{-1}; its simulation curve is shown in Fig. 4a.

(4) Revisiting the fitting of $1/T_1$ vs T data

In summary, variable-band pulse EPR spectroscopy demonstrated the presence of direct process and two-phonon processes, and vibrational spectroscopic studies revealed frequencies of optical phonons and upper limits for T_D. Reasonable simulations of $1/T_1$ vs. T relationships were achieved for MgHOTP and TiHOTP based on this information, which revealed possible spin-lattice relaxation processes. These simulation results help reduce the parameter space for the fitting of $1/T_1$ vs. T data, making it more feasible.

As discussed in the first sub-section, the fitting of $1/T_1$ vs. T data tends to minimize the absolute error of data points with larger $1/T_1$ values by introducing significant relative errors to those with smaller $1/T_1$ values. To elevate this problem, we tried to fit $\log_{10}(1/T_1)$ vs. T data. Specifically, the spin-lattice relaxation mechanisms of TiHOTP and MgHOTP were analyzed by Equation S7 and S8, respectively.

TiHOTP: $\log_{10}\left(\frac{1}{T_1}\right) = \log_{10}\left[A_{Dir}T + A_{Ram}\left(\frac{T}{T_D}\right)^9 \int_0^{\frac{T_D}{T}} x^8 \frac{e^x}{(e^x-1)^2}dx + A_{Loc}\frac{e^{h\nu/k_BT}}{(e^{h\nu/k_BT}-1)^2}\right]$ .... eq. S7

MgHOTP: $\log_{10}\left(\frac{1}{T_1}\right) = \log_{10}\left[A_{Dir}T + A_{Loc,1}\frac{e^{h\nu_1/k_BT}}{(e^{h\nu_1/k_BT}-1)^2} + A_{Loc,2}\frac{e^{h\nu_2/k_BT}}{(e^{h\nu_2/k_BT}-1)^2}\right]$ .... eq. S8

During the fitting, we only fixed $\nu/c = 1489$ cm^{-1} for TiHOTP and fixed $\nu_1/c = 24$ cm^{-1} and $\nu_2/c = 1459$ cm^{-1} for MgHOTP. Other variables were allowed to freely change, and their initial values were taken from optimal simulation results. Decent matches between experimental and fitted $1/T_1$ vs. T data were achieved (Figure 4 and Supplementary Figure 26). The fitted A_{Dir}, A_{Ram}, A_{Loc}, and T_D values of TiHOTP as well as A_{Dir}, $A_{Loc,1}$, and $A_{Loc,2}$ values of MgHOTP are consistent with those obtained from simulations (Supplementary Table 11). Therefore, the fitting results should be reliable.
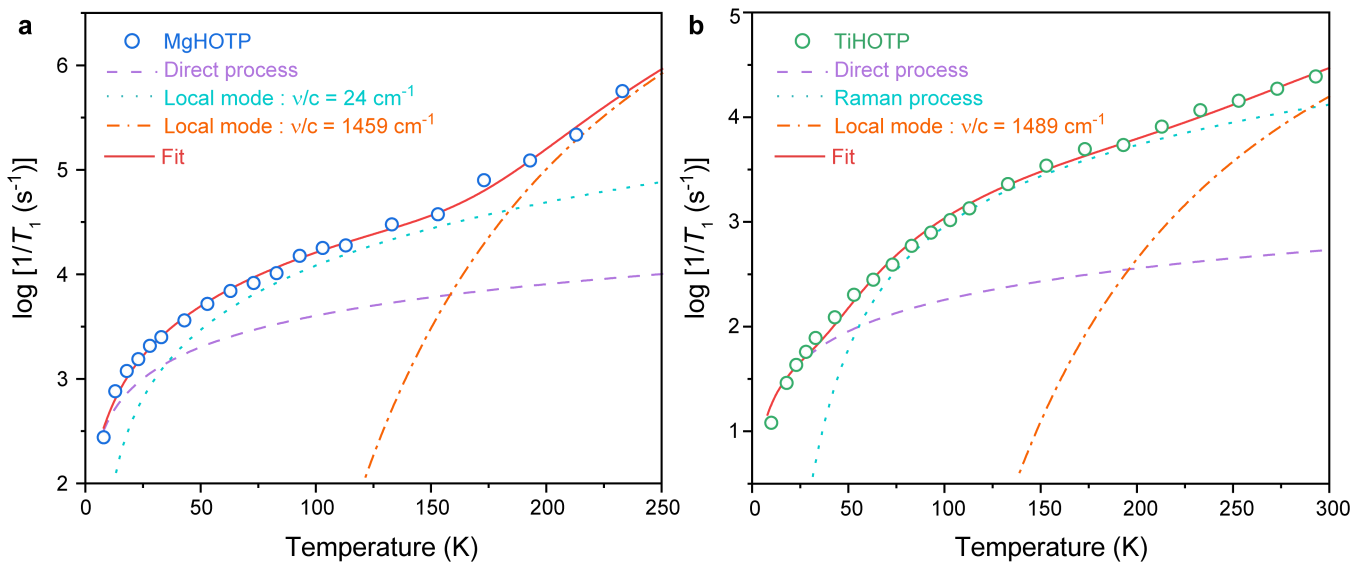
Supplementary Figure 26. Spin-lattice relaxation rates $\log(1/T_1)$ of a, MgHOTP and b, TiHOTP acquired at various temperatures and their fitting results based on eq. S8 and eq. S7. Circles represent experimental data. Purple dash lines represent contributions from direct processes. Light blue dot lines represent contributions from the local-mode process driven by the 24 cm^{-1} optical phonon for MgHOTP or the Raman process for TiHOTP. Orange dash-dot lines represent contributions from local-mode processes driven by C−O stretches in semiquinone moieties. Red solid lines represent the sum of all relaxation processes.

Supplementary Table 11. Simulated spin-lattice relaxation parameters of MQFs.[a]

MQF	Figure	A_{Dir} $(K^{-1}\cdot s^{-1})$	A_{Ram} (s^{-1})	m	T_D (K)	$A_{Loc,1}$ (s^{-1})	ν_1/c (cm^{-1})	$A_{Loc,2}$ (s^{-1})	ν_2/c (cm^{-1})
MgHOTP	Fig.4a (fitting)	40(3)	/	/	/	$1.5(1)\times10^3$	24	$3.7(4)\times10^9$	1459
	Fig.S23a	38	/	/	/	1.2×10^3	24	4.0×10^9	1459
	Fig.S21a	70	2.0×10^{-6}	4.8	/	/	/	/	/
	Fig.S25a	28	1000	/	10	/	/	2.68×10^8	1459
	Fig.S25b	38	1	2	/	/	/	2.32×10^8	1459
	Fig.S25c	35	/	/	/	1.5×10^3	24	2.72×10^7	697
	Fig.S25d	40	/	/	/	1.9×10^3	24	4.70×10^{14}	3350
	Fig.S25e	60	/	/	/	1.5×10^4	90	4.02×10^9	1459
	Fig.S25f	70	/	/	/	6.2×10^4	177	4.00×10^9	1459
TiHOTP	Fig.4b (fitting)	1.8(3)	$1.0(7)\times10^5$	/	$3.0(7)\times10^2$	$2(1)\times10^7$	1489	/	/
	Fig.S23b	1.6	7.2×10^4	/	263	2.0×10^6	1489	/	/
	Fig.S21b	1.5	1.55×10^{-4}	3.3	/	/	/	/	/
	Fig.S24a	1.6	1.78×10^4	/	263	1.8×10^4	310	/	/
	Fig.S24b	1.5	6.78×10^4	/	263	9.0×10^4	714	/	/
	Fig.S24c	1.6	4.96×10^4	/	263	2.0×10^6	1391	/	/
	Fig.S24d	0	0.09	2	/	2.5×10^6	1489	/	/
	Fig.S24e	4.09	/	/	/	4.4×10^4	310	1.22×10^7	1489
MgHOTP-D$_2$O	Fig.5b (fitting)	$4(1)\times10^2$	/	/	/	$1.1(3)\times10^3$	15	/	/
	Fig.S31 (fitting)	$4(1)\times10^2$	2.4(5)	2	/	/	/	/	/

MQF	Figure	A_{Direct} $(K^{-1}\cdot s^{-1})$	$A_{Loc,1}$ (s^{-1})	ν_1/c (cm^{-1})	A_{therm} (s^{-1})		E_a (K)	τ_c (s^{-1})	ω (Hz)
TiHOTP	Fig.S24f	1.6	3.4e6	1500	6.89×10^{16}		236	7.08×10^{-8}	9.74×10^9

[a]Data shown with parathesis are fitting results. Other data are simulation results.

**Supplementary Table 12.** Spin-lattice relaxation parameters of selected molecular electron spin qubits.

| Spin qubit[c]	A_{Dir} ($K^{-1} \cdot s^{-1}$)	A_{Raman} (s^{-1})	T_D (K)	A_{Loc} (s^{-1})	v/c (cm^{-1})	T_1 (μs)[b]	Reference
Cu $(Me_2Nac)_2$ (1%)	39	1.5e6	75	1.85×10^8	290	0.47	17
Cu$(acacen)_2$ (1%)	13.8	7e5	63	6×10^6	213	2.43	
Cu(tmtaa) (1%)	18	2.7e5	81	1.1×10^7	328	8.71	
$[V(C_6H_4S_2)_3]^{2-}$ (0.5%)	4.7×10^3	5×10^8	98	5.4×10^9	275	2.67	29
$[Cu(C_6H_4S_2)_2]^{2-}$ (0.5%)	4.8×10^3	1.4×10^8	94.9	2.6×10^9	488	34.80	
$[V(C_6H_4Se_2)_3]^{2-}$ (0.5%)	5.1×10^2	5.1×10^8	71	3.14×10^9	161	1.39	
$[Cu(C_6H_4Se_2)_2]^{2-}$ (0.5%)	2.25×10^3	2.1×10^8	89	3.1×10^9	343.9	5.72	
$Cu_{0.1}$-MOF-525	32	2.37×10^5	77	7×10^6	198.08	9[b]	30
$Cu_{0.1}$-PCN -223	51	1.64×10^5	74	5×10^6	189.74	9[b]	
$0.2C_{60}$@$Cu_{0.1}$-PCN-223	29	2.22×10^5	82	4×10^6	195.30	9[b]	
$1.0C_{60}$@$Cu_{0.1}$-PCN-223	32	1.77×10^5	94	6×10^6	200.87	9[b]	
$^{13}C_1$-PTMTC	0.22	1.4×10^4	160	4.9×10^5	590.78	2000[b]	31
$^{13}C_1$-dFT	0.6	1.3×10^4	160	1.1×10^6	695.03	2000[b]	
pegylated nitroxide diradicals	5.4	1.5×10^4	100	1.3×10^7	660.28	800[b]	32
2,5PSQ	0.4	1.08×10^4	150	8.9×10^4	417.02	1000[b]	33
2,5tASQ	0.41	1.24×10^4	150	1.07×10^5	417.02	1000[b]	
2,5tBSQ	0.41	1.28×10^4	150	1.10×10^5	417.02	1000[b]	
2,6tBSQ	0.56	1.47×10^4	150	1.28×10^5	417.02	1000[b]	
THSQ	0.1	1.5×10^4	150	1.29×10^5	417.02	1300[b]	

[a]Temperature is between 80-90 K.

[b]Value estimated from a figure in the reference.

[c]Me_2Nac = N,N′-dimethyl-4-amino-3-penten-2-imine; acacen = bis(acetylacetone)ethylenediamine; tmtaa = tetramethyltetraazaannulene; $C_6H_4S_2$ = dithiocatecholate; $C_6H_4Se_2$ = diselenocatecholate; PTMTC = perchlorotriarylmethyl tricarboxylic acid radical; dFT = perdeuterated Finland trityl; 2,5PSQ = 2,5-di-phenyl-1,4-benzosemiquinone; 2,5tASQ = 2,5-di-t-amyl-1,4-benzosemiquinone; 2,5tBSQ = 2,5-di-t-butyl-1,4-benzosemiquinone; 2,6tBSQ = 2,6-di-t-butyl-1,4-benzosemiquinone; THSQ = tetrahydroxy-1,4-benzosemiquione.

12. Deuteration experiments
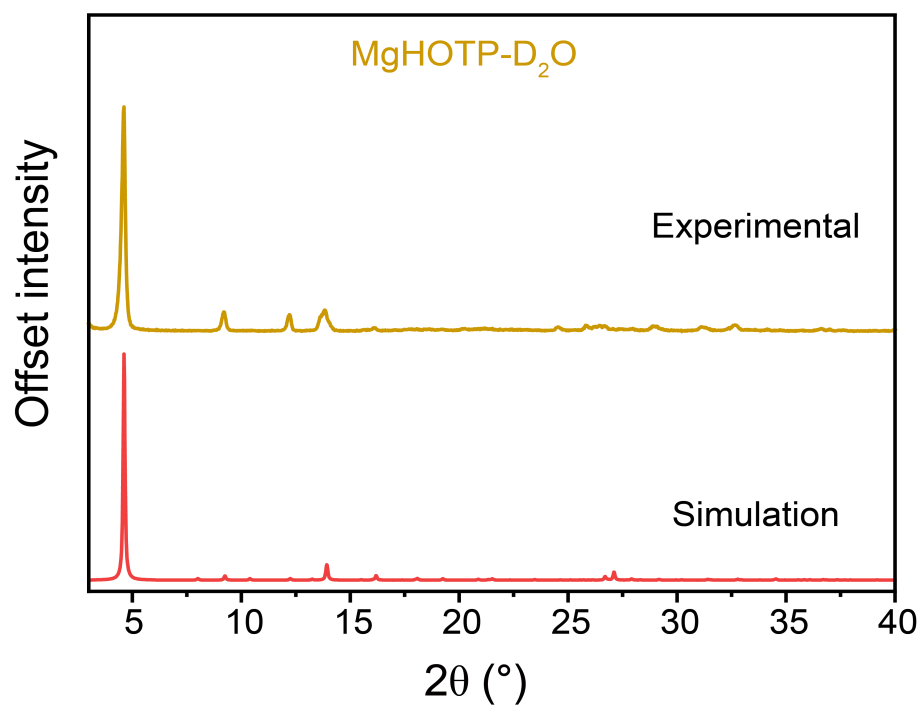
Supplementary Figure 27. Experimental PXRD pattern of MgHOTP-D$_2$O. The red line represents the simulated pattern based on the single crystal structure of MgHOTP.
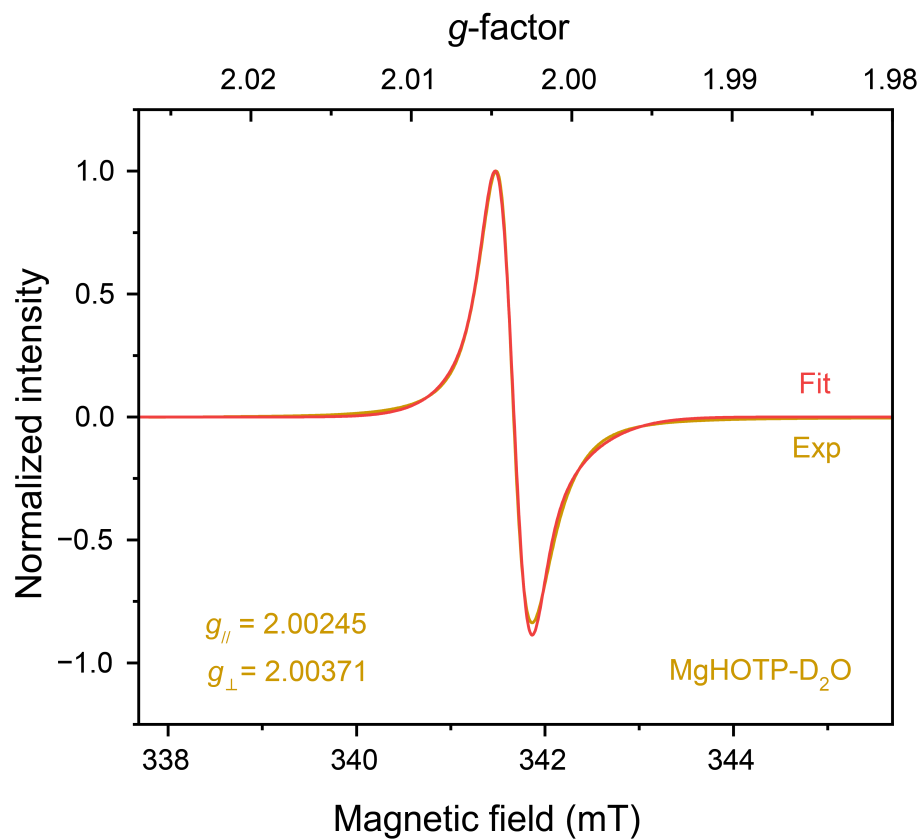
Supplementary Figure 28. X-band CW EPR spectrum of MgHOTP-D₂O. The red line represents fitting results.
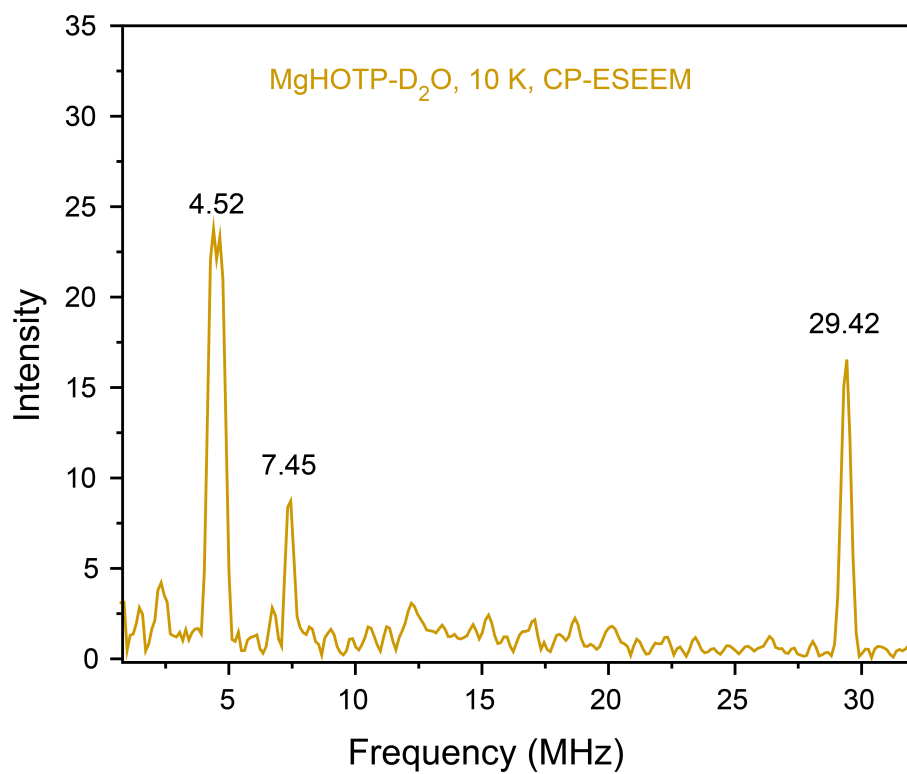
Supplementary Figure 29. Frequency-domain CP-ESEEM spectra of MgHOTP-D$_2$O. The peaks at 4.52 MHz, 7.45 MHz, and 29.42 MHz asre attributed to ^{2}H, ^{13}C, and ^{1}H, respectively.

Mechanistic analysis on spin decoherence (Supplementary Note 12)

The temperature dependence of T_m of MgHOTP-D_2O is comparable to that of MgHOTP below 173 K. Above 173 K, the T_m of MgHOTP-D_2O increases with rising temperatures. Such thermal behavior indicates the presence of two motion-induced decoherence processes in MgHOTP-D_2O at different temperatures. The upturn of T_m in the high temperature region prevents us from performing the abovementioned quantitative analysis with Equation S1, so we could not identify exact peak temperatures of these processes (Supplementary Figure 30). Nonetheless, these results indicate that the motion in MgHOTP stems from proton tunneling in hydrogen bonds. As deuterium is twice as heavy as hydrogen, deuterium tunneling is much slower than proton tunneling and needs a higher temperature to activate[34]. Therefore, we assign the high-temperature motion to the deuterium tunneling in O−D···O hydrogen bond between coordinating D_2O and HOTP, and rationalized the low-temperature motion to the proton tunneling in O−H···O hydrogen bond between residual coordinating H_2O and HOTP.
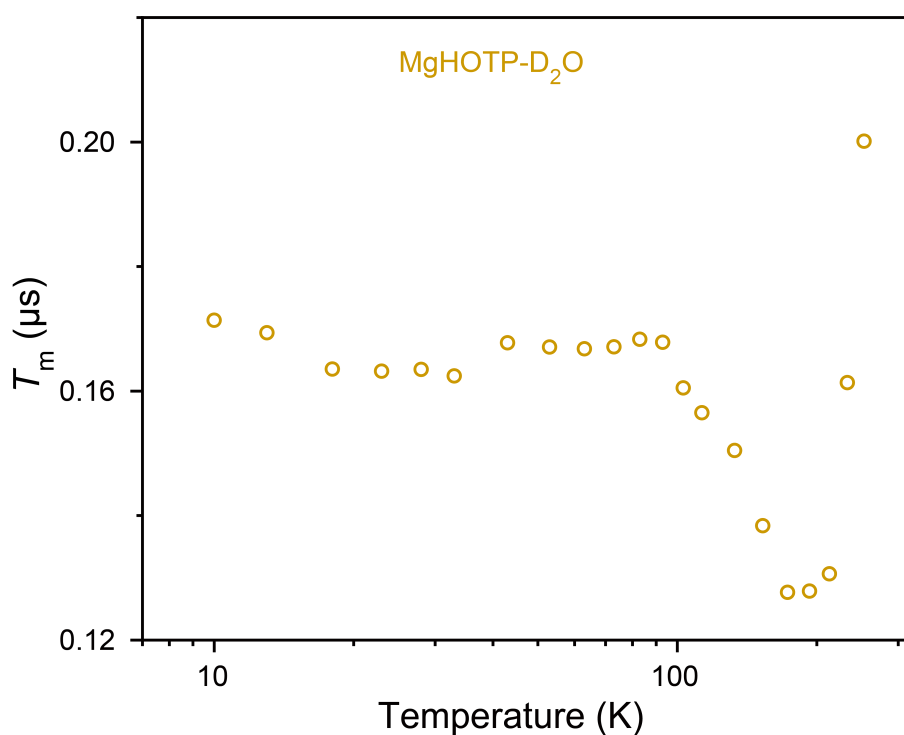
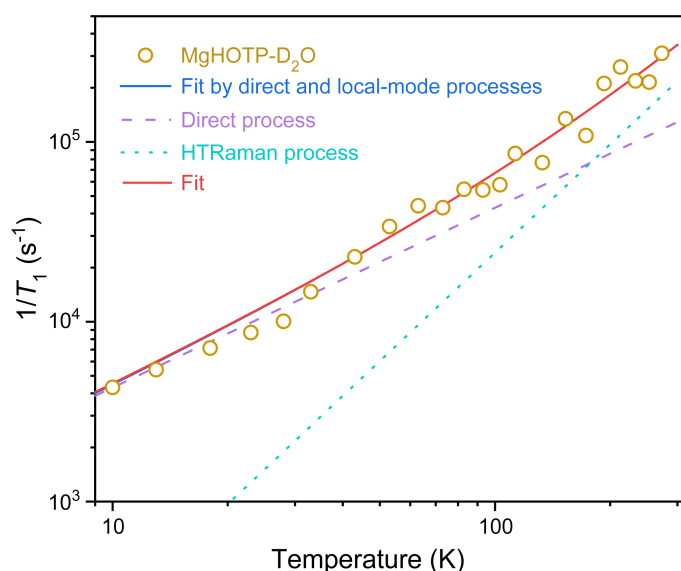**Supplementary Figure 30.** T_m MgHOTP-D_2O at various temperatures.

Mechanistic analysis on spin-lattice relaxation

As discussed in the main text, MgHOTP-D$_2$O should exhibit lower T$_D$ than MgHOTP, and its lowest-frequency optical phonon is at 15 cm^{-1}. Hence, both Raman process and the local-mode process with v/c = 15 cm^{-1} reach their high-temperature limits. Both processes may be involved in the spin-lattice relaxation, and their contributions cannot be distinguished. Meanwhile, the direct process should participate in the spin-lattice relaxation. Thus, we tried to fit the 1/T_1 vs. T data of MgHOTP-D$_2$O with Equation S9 and S10.

$$\text{Local-mode process: } \frac{1}{T_1} = A_{Dir}T + A_{Loc}\frac{e^{h\nu/k_BT}}{\left(e^{h\nu/k_BT}-1\right)^2} \dots\dots\dots\dots\dots\dots\dots\dots\dots\dots\dots\dots \text{eq. S9}$$

$$\text{High-temperature-limit Raman process: } \frac{1}{T_1} = A_{Dir}T + A_{Ram}T^2 \dots\dots\dots\dots\dots\dots\dots \text{eq. S10}$$

Both equations gave decent fitting results (Figure 5b and Supplementary Figure 31). Notably, when using Equation S9, the fitted A$_{Loc}$ value is 1.1 × 10^3 s^{-1}, which is comparable to the A$_{Loc}$ value (1.5 × 10^3 s^{-1}) of the local-mode process with v/c = 24 cm^{-1} for MgHOTP (Supplementary Note 11). Such comparability indicates that the deuteration does not alter the DOS of the lowest-frequency optical phonon. The lower frequency of this optical phonon significantly improves its associated relaxation rate. In addition, local-mode processes driven by high-frequency optical phonons (e.g. the one at 1459 cm^{-1}) are not needed in the fitting, consistent with the lack of upturn of 1/T_1 at high temperatures.

Supplementary Figure 31. Fitting of 1/T_1 vs T relationship for MgHOTP-D$_2$O with a combination of direct process and Raman process at its high-temperature limit.
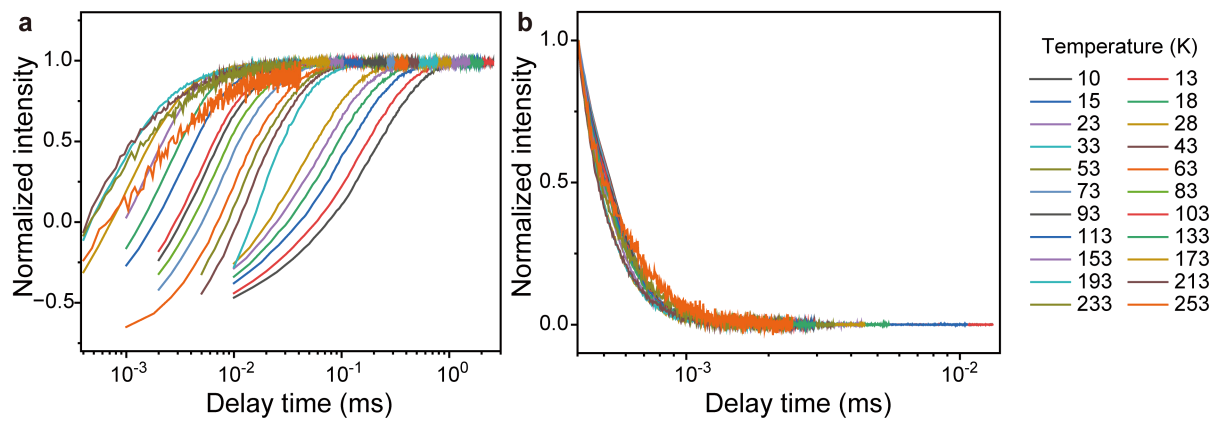
Supplementary Figure 32. a, Inversion recovery curves of MgHOTP-D$_2$O at various temperatures. b, Hahn echo decay curves of MgHOTP-D$_2$O at various temperatures.

Supplementary Table 13. T_1 and T_m of MgHOTP-D$_2$O at various temperatures.

Temperature (K)	T_1 (µs)	T_s (µs)	T_m (ns)
10	2.257 (6) × 10^2	3.3 (2) × 10^1	1.714 (5) × 10^2
13	1.85 (1) × 10^2	4.9 (2) × 10^1	1.694 (4) × 10^2
18	1.40 (2) × 10^2	5.6 (3) × 10^1	1.635 (3) × 10^2
23	1.15 (2) × 10^2	4.8 (3) × 10^1	1.632 (3) × 10^2
28	9.9 (4) × 10$^{1.}$	4.8 (2) × 10^1	1.635 (3) × 10^2
33	6.8 (1) × 10^1	2.7 (1) × 10^1	1.624 (3) × 10^2
43	4.4 (1) × 10^1	1.53 (2) × 10^1	1.677 (4) × 10^2
53	2.96 (6) × 10^1	1.14 (2) × 10^1	1.671 (3) × 10^2
63	2.27 (3) × 10^1	7.4 (2)	1.679 (3) × 10^2
73	2.32 (7) × 10^1	8.6 (2)	1.671 (3) × 10^2
83	1.83 (3) × 10^1	6.36 (8)	1.683 (3) × 10^2
93	1.85 (5) × 10^1	5.80 (6)	1.678 (4) × 10^2
103	1.73 (5) × 10^1	5.01 (5)	1.605 (4) × 10^2
113	1.16 (3) × 10^1	4.11 (5)	1.565 (3) × 10^2
133	1.31 (5) × 10^1	3.20 (2)	1.504 (3) × 10^2
153	7.4 (4)	2.36 (2)	1.384 (3) × 10^2
173	9.2 (4)	1.65(1)	1.276 (4) × 10^2
193	4.7 (1)	1.07 (2)	1.279 (5) × 10^2
213	3.83 (7)	0.714 (9)	1.31 (1) × 10^2
233	4.6 (1)	0.62 (2)	1.61 (1) × 10^2
253	4.7 (2)	0.74 (4)	2.00 (2) × 10^2

References

1. Yeap, G.-Y. *et al.* Synthesis and liquid crystalline studies of disc-shaped molecule on azo-bridged benzothiazole-phenyl ethers. *J Mol. Liq.* 223, 734–740 (2016).

2. Wang, S. *et al.* Six-arm star polymer based on discotic liquid crystal as high performance all-solid-state polymer electrolyte for lithium-ion batteries. *J Power Sources* 395, 137–147 (2018).

3. Sun, L. *et al.* Room-temperature quantitative quantum sensing of lithium ions with a radical-embedded metal–organic framework. *J Am. Chem. Soc.* 144, 19008–19016 (2022).

4. Nguyen, N. T. T. *et al.* Three-dimensional metal-catecholate frameworks and their ultrahigh proton conductivity. *J Am. Chem. Soc.* 137, 15394–15397 (2015).

5. Stoll, S. & Schweiger, A. EasySpin, a comprehensive software package for spectral simulation and analysis in EPR. *J. Magn. Reson.* 178, 42–55 (2006).

6. Hartmann, S. R. & Hahn, E. L. Nuclear Double Resonance in the Rotating Frame. *Phys. Rev.* 128, 2042–2053 (1962).

7. Wilson, C. B., Qi, M., Han, S. & Sherwin, M. S. Gadolinium spin decoherence mechanisms at high magnetic fields. *J. Phys. Chem. Lett.* 14, 10578–10584 (2023).

8. Lim, H.-J., Welinski, S., Ferrier, A., Goldner, P. & Morton, J. J. L. Coherent spin dynamics of ytterbium ions in yttrium orthosilicate. *Phys. Rev. B* 97, 064409 (2018).

9. Schott, S. *et al.* Polaron spin dynamics in high-mobility polymeric semiconductors. *Nat. Phys.* 15, 814–822 (2019).

10. Eggeling, A., Soetbeer, J., Fábregas-Ibáñez, L., Klose, D. & Jeschke, G. Quantifying methyl tunneling induced (de)coherence of nitroxides in glassy ortho -terphenyl at low temperatures. *Phys. Chem. Chem. Phys.* 25, 11145–11157 (2023).

11. Jackson, C. E. *et al.* Impact of counter ion methyl groups on spin relaxation in [V(C$_6$H$_4$O$_2$)$_3$]$^{2-}$. *J. Phys. Chem. C* 126, 7169–7176 (2022).

12. Horsewill, A. J. Quantum tunnelling in the hydrogen bond. *Prog. Nucl. Magn. Reson. Spectrosc.* 52, 170–196 (2008).

13. Atzori, M. *et al.* Room-temperature quantum coherence and Rabi oscillations in vanadyl phthalocyanine: toward multifunctional molecular spin qubits. *J. Am. Chem. Soc.* 138, 2154–2157 (2016).

14. Bader, K. *et al.* Room temperature quantum coherence in a potential molecular qubit. *Nat. Commun.* 5, 5304 (2014).

15. Zadrozny, J. M., Niklas, J., Poluektov, O. G. & Freedman, D. E. Millisecond coherence time in a tunable molecular electronic spin qubit. *Acs. Central. Sci.* 1, 488–492 (2015).

16. Lagostina, V. *et al.* Magnetic and relaxation properties of vanadium(IV) complexes: an integrated ^{1}H relaxometric, EPR and computational study. *Inorg. Chem. Front.* 10, 1999–2013 (2023).

17. Amdur, M. J. *et al.* Chemical control of spin–lattice relaxation to discover a room temperature molecular qubit. *Chem. Sci.* 13, 7034–7045 (2022).

18. Wojnar, M. K., Laorenza, D. W., Schaller, R. D. & Freedman, D. E. Nickel(II) metal complexes as optically addressable qubit candidates. *J. Am. Chem. Soc.* 142, 14826–14830 (2020).

19. Laorenza, D. W. *et al.* Tunable Cr^{4+} molecular color centers. *J. Am. Chem. Soc.* 143, 21350–21363 (2021).

20. Pang, S.-M., Lv, Y.-P. & Zhang, J. Spurious signals identification in Brillouin light scattering spectrum. *J. Raman Spectrosc.* 55, 1019–1026 (2024).

21. Jarmola, A., Acosta, V. M., Jensen, K., Chemerisov, S. & Budker, D. Temperature- and magnetic-field-dependent longitudinal spin relaxation in nitrogen-vacancy ensembles in diamond. *Phys. Rev. Lett.* 108, 197601 (2012).

22. Gregson, M. *et al.* A monometallic lanthanide bis(methanediide) single molecule magnet with a large energy barrier and complex spin relaxation behaviour. *Chem. Sci.* 7, 155–165 (2015).

23. Atzori, M. *et al.* Quantum coherence times enhancement in vanadium(IV)-based potential molecular qubits: the key role of the vanadyl moiety. *J. Am. Chem. Soc.* 138, 11234–11244 (2016).

24. Atzori, M. *et al.* Structural effects on the spin dynamics of potential molecular qubits. *Inorg. Chem.* 57, 731–740 (2018).

25. Oanta, A. K. *et al.* Electronic spin qubit candidates arrayed within layered two-dimensional polymers. *J. Am. Chem. Soc.* 145, 689–696 (2023).

26. Shrivastava, K. N. Theory of Spin–Lattice Relaxation. *Phys. Stat. Sol. (b)* 117, 437–458 (1983).

27. Gu, L. & Wu, R. Origin of the anomalously low Raman exponents in single molecule magnets. *Phys. Rev. B* 103, 014401 (2021).

28. Zhou, A., Sun, Z. & Sun, L. Stable organic radical qubits and their applications in quantum information science. *The Innovation* 5, 100662 (2024).

29. Fataftah, M. S. *et al.* Metal–ligand covalency enables room temperature molecular qubit candidates. *Chem. Sci.* 10, 6707–6714 (2019).

30. Vujević, L. *et al.* Improving the molecular spin qubit performance in zirconium MOF composites by mechanochemical dilution and fullerene encapsulation. *Chem. Sci.* 14, 9389–9399 (2023).

31. Moore, W., Huffman, J. L., Driesschaert, B., Eaton, S. S. & Eaton, G. R. Impact of chlorine substitution on electron spin relaxation of a trityl radical. *Appl. Magn. Reson.* 53, 797–808 (2022).

32. Sato, H. *et al.* Impact of electron−electron spin interaction on electron spin relaxation of nitroxide diradicals and tetraradical in glassy solvents between 10 and 300 K. *J. Phys. Chem. B* 112, 2818–2828 (2008).

33. Kathirvelu, V., Sato, H., Eaton, S. S. & Eaton, G. R. Electron spin relaxation rates for semiquinones between 25 and 295 K in glass-forming solvents. *J. Magn. Reson.* 198, 111–120 (2009).

34. Xue, Q., Horsewill, A. J., Johnson, M. R. & Trommsdorff, H. P. Isotope effects associated with tunneling and double proton transfer in the hydrogen bonds of benzoic acid. *J. Chem. Phys.* 120, 11107–11119 (2004).